# CONTENTS

# CHAPTER 3

# THIN FILMS OF LI@$C_{60}$

## 3.1 Introduction

Endohedral fullerenes are an exciting class of fullerene-based materials, expected to have many interesting electronic and optical properties. Metal-containing fullerenes are of particular interest due to the possibility of tailoring the electronic properties of the fullerenes by adding different electronic donor atoms. Applications as three-dimensional organic conductors and even high temperature superconductors have been suggested for the metallofullerenes. However, the thorough characterisation of these materials has been hampered due to the difficulty to obtain large amounts of purified material. Li@$C_{60}$ was the first metal-containing endohedral $C_{60}$ fullerene successfully synthesised in macroscopic quantities [TKL96, Tel98]. The material can be separated from $C_{60}$ and purified to better than 95% content [Kra98]. In the work presented in this chapter, we studied the thin film preparation conditions, the optical properties and excitation dynamics in thin films of endohedral Li@$C_{60}$ and the phototransformation process of the material.

An outline of the present status of endohedral fullerene research is given in Section 3.2. The Section 3.3 describes the production and purification methods for the production of Li@$C_{60}$ and the theoretical predictions for the properties of this molecule. The following section presents our research concerning the thermal stability of the molecule and the possibility to deposit it as thin films by sublimation. The optical properties of the thin films of Li@$C_{60}$ are discussed in Section 3.4, in comparison with films of $C_{60}$. The excitation dynamics in films of $C_{60}$ and Li@$C_{60}$ are studied in Section 3.6. Li@$C_{60}$ can be polymerised by irradiation with visible light, similar to the $C_{60}$, as shown in Section 3.7. The conclusions are presented in Section 3.8.

## 3.2 Endohedral fullerenes

The possibility of doping fullerenes by inserting atoms into the cage has been suggested already in the first article on Buckminsterfullerene, by Kroto et al. [KHB85]. The unique cage-like structure of fullerenes encloses a central cavity that can accommodate a wide range of atoms. The first endohedral fullerene, La@C$_{60}$, was found in the mass spectra of clusters produced by Heat et al. with laser vaporisation of a La-impregnated graphite disk in a pulsed supersonic nozzle [HBZ85]. Three years later, the same group presented evidence for the formation of K@C$_{60}$ and Cs@C$_{60}$ [WEB88]. In 1991, Chai et al. [CGJ91] reported the first macroscopic production of La@C$_{82}$ metallofullerenes and introduced the use of the "@" symbol for specifying the endohedral nature of the compounds. Since then, a large variety of endohedral fullerenes has been synthesised. They can be classified, according to the nature of the encapsulated atom, in rare gas-, group V element- and metallo-fullerenes.

**Noble gas – endofullerenes.** Noble gas atoms inside a fullerene ideally are not interacting with the fullerene electrons. These types of endofullerenes are thus considered to be analogues of isotopes of the fullerenes. Noble gas atoms (He, Ne, Ar, Kr, Xe) can be introduced into fullerene molecules by treating the fullerene with the gas under a temperature of 650 °C and pressure of 3400 atm [SJV93, SCJ96]. A total endohedral content of less than ~ 0.5% can be achieved under these conditions [YSK99]. The separation of 0.14 mg of 90% pure Kr@C$_{60}$ by four passes through a high performance liquid chromatograph has also been reported in [YSK99]. The fraction of endohedral fullerenes is determined by heating the material at ~ 1000 °C in order to release the gas, which is analysed with a mass spectrometer. The high temperature necessary for the release of the gas atoms is taken as evidence for their encapsulation. The formation of the endohedral species has been explained by an "open window" mechanism, in which one or more of the carbon-carbon bonds of the cage open and reclose, which allows the penetration of the cage in a thermodynamic equilibrium at fairly low collision energies [SCJ96]. The synthesis of endohedral compounds Xe@C$_{60}$ and Kr@C$_{60}$ has been reported from a nuclear reaction recoil process, but no clear evidence or discussion about the endohedral nature of the products was given in this work [OOS98].

**Group V – endofullerenes.** The group-V atoms encapsulated in fullerenes show an ideal trapping behaviour: these highly reactive atoms are uncharged, unbound and stay in their ground state in the centre of the fullerene. The endohedrals are produced by vapour deposition of fullerenes on a substrate and simultaneous irradiation with an intense N or P ion beam [AMP96, DHP99]. Despite the very low yield of endohedral species (0.01%) and a lack of an efficient purification procedure, the endohedral nature of these molecules was confirmed by electron paramagnetic resonance (EPR) studies, due to the paramagnetism of the encapsulated atoms. Production of Sb@$C_{60}$ by nuclear recoil has also been reported [OOS01].

**Metallo-endofullerenes.** The largest class of endohedral fullerenes is, with no doubt, the class of metallofullerenes. The increased interest in these compounds has been stimulated by the discovery that films of $C_{60}$, exohedrally doped with alkali metals, are conducting at room temperature [HHR91] and superconducting at temperatures of 18 – 33 K [HRH91, TES91, KCL91]. Encapsulation of the metal atoms is expected to be useful for the tailoring of the electronic properties of the fullerenes through charge transfer to the cage, while providing an increased chemical stability of the compounds as compared to their exohedral counterparts.

Alkali metals (Li, Na, K, Cs), Group 2 (Ca, Sr, Ba), transition metals (Sc, Y, La, Ti, Zr, Hf, Fe, Co, Ni) and most of the lanthanide series elements have been successfully encapsulated into a fullerene cage [DDE96, LiS00]. The laser vaporisation method first used by Chai et al. [CGJ91], sometimes called “laser furnace” due to the fact that the reaction chamber is heated up to ~ 1200 °C, as well as the Krätschmer-Huffman arc-evaporation technique, in which the arc burns a composite rod made from a metal oxide / carbide and graphite, are most widely used for the synthesis of endohedral metallofullerenes. Encapsulation of one, two or three atoms has been achieved by using these methods. More recently, even trimetallic nitride - fullerene clusters of the type $A_nB_{n-3}N@C_{2x}$, with n = 0-3, x = 34, 39, 40 and A and B group III and rare-earth metals were formed with the arc method [DSC00]. The efficiency for the production of endohedral metallofullerenes using these methods is normally below 1% from the original soot [LiS00]. Although the M@$C_{60}$ species is thought to be the most common in the soot, extraction by sublimation or solvent methods was, over several years, only successful with M@$C_{82}$, with lesser amounts of $M_{2,3}@C_{82}$ and $M_x@C_n$, with x = 1,2 and 3 and n = 72, 74 and 84 [DDE96]. Therefore, most of the theoretical and experimental work has been concentrated on the study of these higher-mass metallofullerenes. Efficient extraction with aniline of some M@$C_{60}$, where M = Y, La, Ce, Pr, Nd, Gd, Ca, Sr, Ba, Dy, Eu and Er has been reported by Kubozono et al. [KMT96]. Further purification by combining sublimation and high performance liquid chromatography (HPLC) has recently enabled separation of macroscopic quantities of Eu@$C_{60}$ [IKK00], Er@$C_{60}$ [OSS00] and Dy@$C_{60}$ [KKT01]. It is still an open question whether the fullerene cage builds up around the atom(s) in these production processes, or the atom penetrates the cage through an "open window" mechanism. The formation of La@$C_{82}$ was described by a coalescence reaction between La, $C_{60}$ and smaller carbon clusters by Saito and Sawada [SaS92]

A new method for the production of endohedral Li@$C_{60}$ was introduced by Campbell et al. in 1996 [TKL96], based on the irradiation of $C_{60}$ films with a low energy ion beam. This method has also been proven to be efficient for the incorporation of up to a few percents of other alkali metals – Na, K, Rb [CTK97, Tel97]. Three possible encapsulation mechanisms have been proposed, in analogy with gas-phase collision experiments: the penetration through a hexagon of the fullerene cage, the cage distortion under the ion impact and the transient bond-breaking or "open window" mechanism [KTG98]. A typical conversion efficiency of $C_{60}$ to Li@$C_{60}$ of up to 30% was obtained under optimised conditions. Material with better than 90% purity was produced by extraction with carbon disulphide followed by HPLC purification. The material properties were investigated mainly by infrared and UV-VIS spectroscopy [GKK97, KTG97, KGB99, Kra98]. Only a few preliminary experiments have been carried out on vapour-deposited films of Li@$C_{60}$ [Kra98].

**Intramolecular charge transfer.** Many specific features of the metallofullerenes are rooted in the electron donation to the fullerene cage by the metal atom(s). This charge transfer determines the stability and electronic properties of the molecules. Several numerical studies predicted that the encapsulated metal atom can transfer valence electrons to the fullerene and stabilises in an off-center equilibrium position, resulting in a net electric dipole moment for the molecule [LiT94, PKW94, ToL95, BrE98, CFH98, AnC98, AKH98]. Clougherty and Anderson [ClA98] explained the spontaneous polarisation of endohedrally metal-doped fullerenes as arising from a Jahn-Teller effect. Acting as an electron donor to the three fold degenerate $t_{1u}$ states of $C_{60}$, the metal atom induces a Jahn-Teller splitting that drives it away from the centre. The calculations concerning Li@$C_{60}$ are discussed in Section 3.3.2.

**Experimental characterisation of endohedral fullerenes.** Most of the experiments testing the endohedral nature of the metallofullerenes are based on laser photodissociation. In such an experiment, $C_2$ units are removed from the fullerene shell, yielding smaller endofullerenes in a process called "shrink wrapping" of the carbon cage around the endohedral core. Other characterisation methods require larger, purified amounts of the endohedral material, unless the method is highly sensitive to the dopant species, as the case for the EPR signals from N and P atoms inside a $C_{60}$ cage [DHP99] and nuclear magnetic resonance spectrum of $^3$He inside $C_{60}$ and $C_{70}$ fullerenes [SCJ96]. EPR is a highly valued technique for characterising the charge transfer for the endohedral dopants, via line shape and hyperfine interaction studies. It has been successfully used for the characterisation of several compounds $M@C_{82}$, with M = La, Sc, Y [LiS00]. Synchrotron powder diffraction measurements were performed on $Y@C_{82}$ and $Sc@C_{82}$ [LiS00]. High resolution scanning tunnelling microscopy studies provided strong evidence for a nearly spherical shape for single molecules of $Sc@C_{74}$, $Sc_2@C_{74}$, $Sc_2@C_{84}$, meaning that the metal species is within the fullerene cage. Similar results were obtained for $Y@C_{82}$ and $Gd@C_{82}$ on Cu(111) surfaces [SWX96]. UV-VIS-NIR and vibrational spectroscopy were also reported on several endohedral species $M@C_{60}$, with M = Li, Dy, Eu [TKL96, KTG97, JKL97, Kra98, IKK00, KKT01], $M_2@C_{80}$ (M = La, Pr, Ce) and $M@C_{82}$, with M = Pr, La, Y, Gd, Nd, Tb, Lu and Ce [LiS00]. A general trend in the UV-VIS-NIR spectra is the onset of the absorption at lower energies compared to the respective undoped fullerenes. Incorporation of a single trivalent ion in $C_{82}$ induces a new broad absorption band peaking at 1400 nm, attributed to their open-shell electronic structures in the electronic conformation $M^{3+}@C_{82}^{3-}$. A similar absorption band can be seen in $Li@C_{60}$, but only under special preparation conditions, as will be discussed in Section 3.5.2. X-ray absorption near edge structure was studied for $Eu@C_{60}$ and $Dy@C_{60}$ [IKK00, KKT01]. The valence state of the Eu atom inside the $C_{60}$ was determined to be +2, while the valence of Dy, located at an off-centre position of 1.25- 1.30 Å from the centre of the cage, is +3. The first ultraviolet photoemission spectroscopy study was reported in 1993 by Wang et al. [WAC93] on $Ca@C_{60}^-$ in gas phase. The spectrum suggested that Ca donates its two 4s electrons to the $C_{60}$ $t_{1u}$ level. X-ray and UV photoelectron spectroscopy on vapour-deposited films of $La@C_{82}$ indicated a total charge transfer from the La atom to the $C_{82}$ cage [PKW94]. Later measurements of resonant photoemission spectra indicated, though, that the charge transfer is incomplete and about 0.3 of an electron charge is left in the La-valence orbitals [KBC97]. Although in a simple one-electron picture the $La^{+3}@C_{82}^{-3}$ is expected to have metallic character, the compound was found to form a non-metallic solid with the uppermost band centered 0.64 eV below the Fermi level.

## 3.3 Endohedral $Li@C_{60}$

### 3.3.1 Production and purification

A detailed description of the experimental setup and the parametric dependence for the production of the endohedral $Li@C_{60}$ is given in the Ph.D. thesis of R. Tellgmann [Tel97]. The purification of the endohedral fullerenes has been a major part of the Ph.D. work of N. Krawez

[Kra98]. Only a short outline of the general route employed for the production and the purification of the endohedral Li@$C_{60}$ used in the present measurements is given here.

The endohedral fullerene Li@$C_{60}$ is produced by low energy $Li^+$ implantation in $C_{60}$ films following the method introduced by Campbell et al. [TKL96]. Hoechst "Gold Grade" $C_{60}$ is sublimated under high vacuum ($10^{-6}$ mbar) from a quartz oven at 500 °C onto an aluminium foil - coated metal cylinder. The rotation speed of the cylinder is controlled for the deposition of only one monolayer of $C_{60}$ for each rotation. The cylinder is irradiated by a beam of $Li^+$ ions in a perpendicular configuration, which avoids gas phase collisions with the $C_{60}$ vapour beam. The optimum ion beam energy for the production of the endohedral Li@$C_{60}$ was found to be 30 eV [CTK97]. Ions with a higher energy can shoot through and exit the fullerene cage or cause the destruction of the fullerene. The ion current on the substrate is monitored during the irradiation, so that the $Li^+$:$C_{60}$ ratio in the deposited film can be estimated. The total amount of endohedrally doped fullerenes increases with this ratio and a conversion efficiency of better than 50% was obtained for a ratio of 17:1, for the ion irradiation of thin films.

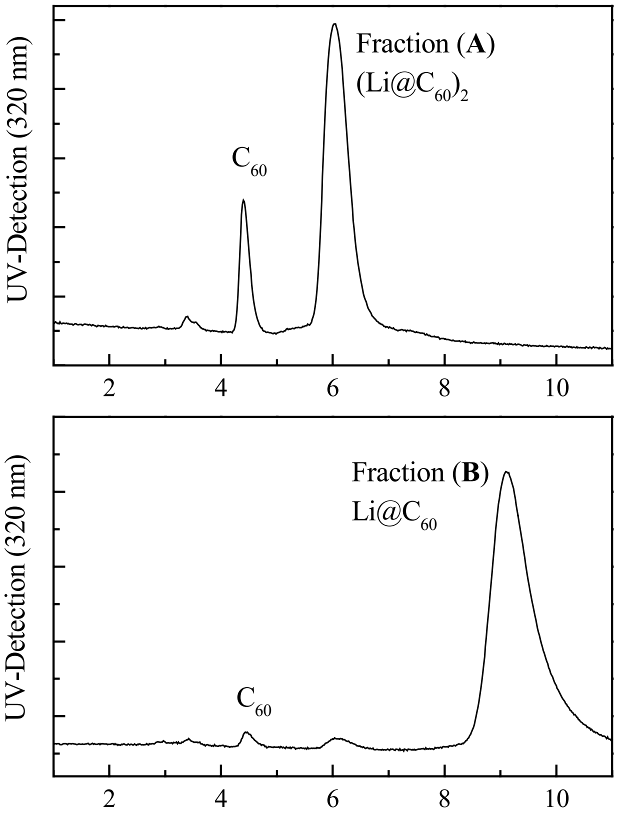

*Fig.3.1.HPLC analysis of the purified endohedral material with a content of more than 95 % Li@$C_{60}$ (E2) and a small fraction of the dimer (Li@$C_{60}$)$_2$ (E1). The solvent impurities (S) and the $C_{60}$ content are further reduced by purging the solid material in hexane.*

For the material used in the present work, a ratio of 1:1 at 30 eV was used for the production of the endohedral Li@$C_{60}$, in order to achieve that more than 90% of the film material is dissolving in carbon disulphide for further purification. Higher $Li^+$:$C_{60}$ ratios dramatically reduce the solubility of the films [GKK97]. A first step of enrichment of Li@$C_{60}$ to about 70% is achieved using anisole, which dissolves mainly $C_{60}$ [Kra98]. Solutions in o-dichlorobenzene (ODBC) are finally purified by HPLC through a Cosmosil 5PBB column.

A typical chromatogram of these solutions shows three well defined peaks: one corresponding to $C_{60}$, with a retention time of 4.4 min, and two endohedral peaks, with retention times of 6 min (Fraction A) and 9.1 min (Fraction B). Fraction A has been assigned to (Li@$C_{60}$)$_2$, by comparison of the retention time and IR spectrum with measurements of the $C_{60}$ dimer, while Fraction B was considered to correspond to the Li@$C_{60}$ monomer [Kra98]. Each endohedral peak was separated in the HPLC procedure, dried and kept under $N_2$ atmosphere at 5 °C for more than one year without any significant decay. The ODBC solvent impurities were reduced by purging the material in hexane. The HPLC trace of this material is presented in Fig.3.1. The HPLC and Laser Desorption Mass Spectrometry (LDMS) analysis of the Fraction B (mainly used in this work) show a fullerene concentration of better than 95% Li@$C_{60}$ (see discussions below and references [GKK97, KTG98]).

### 3.3.2 Intramolecular charge transfer - theoretical predictions

Li and Tománek [LiT94, ToL95] have calculated the interaction between the encapsulated Li atom and the $C_{60}$, using the density functional formalism. This interaction is predominantly ionic, with only a small covalent contribution from the Li2s orbital. Aree et al. [AKH98] have performed ab initio Hartree-Fock calculations for displacements of Li along a trajectory from the center of the cage towards a pentagon, a hexagon, a double or a single bond of the fullerene cage. The Li atom completely ionises to form $Li^+$ at a distance of less than 1 Å from the central position. The electron is transferred from the Li 2s orbital to the $t_{1u}$ LUMO of $C_{60}$ and the charge is distributed almost uniformly over the surface of $C_{60}$. The interaction between Li and $C_{60}$ has ionic character within this distance. When the Li was moved closer to the inner surface of $C_{60}$, the donated electron was continuously transferred back from $C_{60}$ to Li, independent of the chosen trajectory. The partially ionised Li polarises the $C_{60}$ spherical electric field, leading to a distortion in the electron distribution of $C_{60}$ so that the electron density is highest for the carbon atoms located near the trajectory axis. This polarisation effect accounts for the stabilised off-center configuration with the Li atom at about 1.3 Å from the center of the cage, corresponding to a charge transfer of ~ 90%. The equilibrium position of the Li inside the $C_{60}$ was found by Li and Tománek [LiT94, ToL95] to be at a distance of 1.5 Å from the center of the cage, with a stabilisation energy of 0.7 eV. A charge transfer of 30% from the Li atom to the $C_{60}$ cage was estimated for this off-centre displacement. The atom rotates almost freely near a spherical surface of 1.5 Å radius. The $C_{60}$ molecule remains almost unchanged by this charge transfer, the C-C bond lengths increasing by less than 0.01 Å and the total energy decreasing by less than 0.1 eV. The dipole moment of Li@$C_{60}$ in the equilibrium geometry was calculated to be 1.18 D (where 1 D is the dipole moment of an $e^+e^-$ pair separated by 0.208 Å) [ToL95].

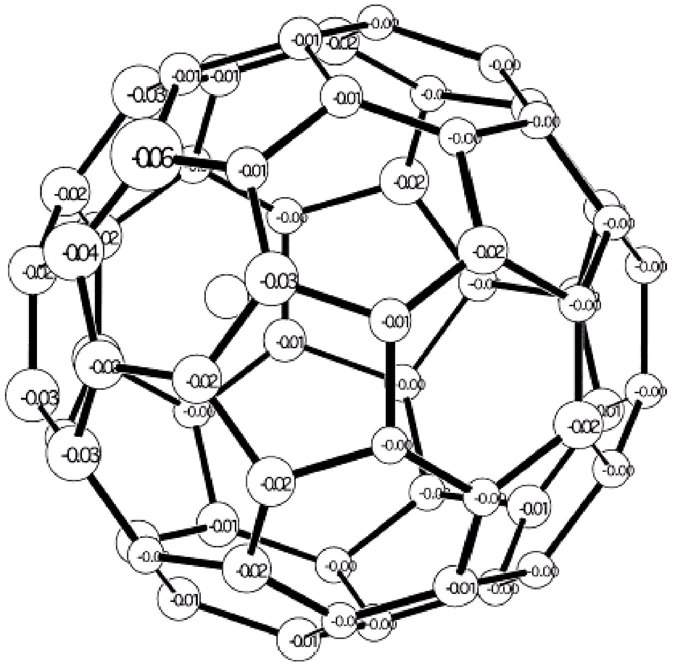

*Fig.3.2. Charge distribution for an equilibrium position of the encapsulated Li atom of 1.5 Å from the cage centre. The size of each carbon atom is proportional to the additional charge [CFH98].*

Campbell et al. [CFH98] calculated a 60% charge transfer from the lithium atom to the fullerene cage, for the same equilibrium distance of 1.5 Å from the centre of the cage. The total dipole moment of the molecule calculated in this work is of the order of 0.2 D. This relatively large difference compared to the value given by Li and Tománek is explained by a more uniform distribution of the extra-charge on the carbon atoms of the fullerene, illustrated in Fig.3.2. A perfect localisation of the charge on one carbon atom would give a dipole moment of the order of 10 D.

While all these theoretical calculations demonstrate that charge transfer from the lithium atom to the fullerene cage is to be expected for the Li@$C_{60}$, the only experimental evidence was found from the absorption spectrum of vapour-deposited films of purified Li@$C_{60}$ [Kra98]. The optical absorption properties of Li@$C_{60}$ will also be discussed in Section 3.7 of the present work. Further evidence for the intramolecular charge transfer, from experiments of transient absorption at 1250 nm, will be presented in Section 3.8.

## 3.4 Thermal stability and sublimation of Li@$C_{60}$ molecules

### 3.4.1 Thermal stability

The thermal stability of Li@$C_{60}$ was investigated by heating the same quantities of material in a quartz crucible under high vacuum at different temperatures and for different times. The material was charged as ODBC solution, dried in air, then degassed for a few hours under high vacuum before being heated. The heated material was then ultrasonicated with ODBC and the soluble fraction was analysed by HPLC. The integrals over the HPLC peaks identified as Li@$C_{60}$, (Li@$C_{60}$)$_2$ and $C_{60}$, which are given in Fig.3.3, show that Li@$C_{60}$ is fairly stable for temperatures up to 150 °C. There is no clear correlation that could indicate a thermal decay of Li@$C_{60}$ into $C_{60}$ up to this temperature. The soluble fraction of Li@$C_{60}$ decreases significantly between 175 and 200 °C. A slight increase of the $C_{60}$ fraction was found for temperatures between 150 and 180 °C, which could be due to the release of Li atoms from $C_{60}$ cages. The dimer fraction is also reduced with increasing temperature, approximately by the same percentage as the monomer. The increase in the $C_{60}$ signal is much smaller than the overall decrease in the endohedral fractions. Two processes are considered for the loss of the endohedral material: the transformation into an insoluble, polymerised phase and the complete destruction of the fullerene cage. Assuming only a simple, unimolecular process for the loss of Li@$C_{60}$, with the reaction rate $k$ given by the Arrhenius relation

$$k = A \cdot e^{-\frac{E_a}{k_B T}}, \tag{3.1}$$

an Arrhenius plot of this decay would give an activation energy as low as 0.4 ± 0.1 eV and a pre-exponential factor $A \approx 9.4\ s^{-1}$. These values are quite close to the values reported in [KGB99] for the thermal decay of Li@$C_{60}$ from the unpurified material. The impurities in the unpurified material, which are the exohedral Li and the residual carbon from a possible destruction of fullerenes due to ion irradiation and the empty $C_{60}$ cages present in the $Li^+$ irradiated $C_{60}$ films, do not catalyse the thermal destruction of the endohedrals.

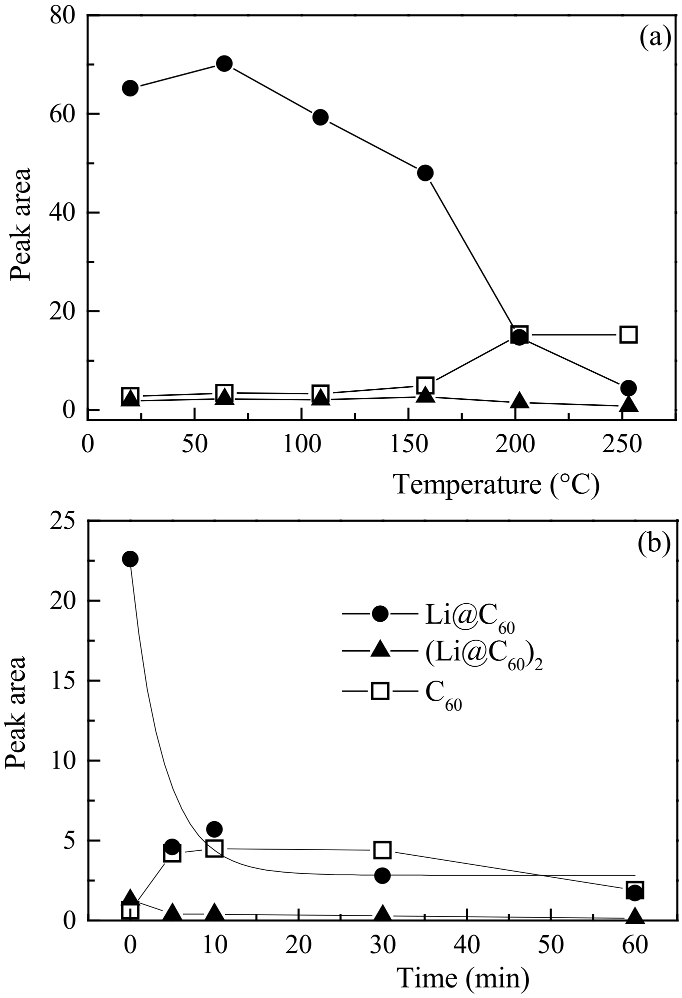

*Fig.3.3. Thermal stability of solid Li@$C_{60}$ under $10^{-5}$ mbar vacuum measured by HPLC analysis of the soluble fraction. In graph (a) equal quantities of the pristine material were heated for one hour at different temperatures, while in (b) equal quantities of pristine material were heated for different periods of time at 220 °C.*

The kinetics of the thermal decay was measured at a temperature of 220°C (Fig.3.3b). A fit using an exponential function $S = s+S_0 \cdot e^{-kt}$ with $S$ the HPLC peak area at a time $t$ of the heating gives a value of ~ $4.3 \cdot 10^{-3}$ $s^{-1}$ for the decay rate $k$. When calculating $k$ from the Arrhenius relation for a temperature of 220 °C, we find a value of $4.8 \cdot 10^{-4}$ $s^{-1}$, which is one order of magnitude smaller than the experimental value. An offset $s$ = 2.8 (equivalent to 12% from the initial peak area) must be included in the fit of the decay with a single exponential function, which means that not all endohedral material is lost in the heating process. This is in good agreement with the report of a constant vapour beam of Li@$C_{60}$ over ~ 20 minutes used for photoionisation measurements and obtained by heating a considerable amount of material at 400 °C in reference [RBH00]. We consider the misfit in the reaction rate and the nonzero offset in the exponential decay to be a clear indication that the thermal decay of the Li@$C_{60}$ is more complex than a unimolecular process. It is very probable that the loss of the Li from the cage and the total destruction of the cage be both catalysed by impurities. An indication for the destruction of the fullerene cage comes from the growth of carbon nanotubes on highly oriented pyrolitic graphite from the Li@$C_{60}$ material.

Nevertheless, the measurement of the kinetics at 220 °C shows that about 75% of the Li@$C_{60}$ material is lost within five minutes. In consequence, an extended heating for the preparation of thin films by sublimation, with a controlled deposition rate, would inherently lead to the thermal loss of most of the material. Because of the high cost of production and the scarcity of the endohedral Li@$C_{60}$, a different deposition technique or special heating strategy must be employed for the preparation of thin films for further experiments.

### 3.4.2 Sublimation of Li@$C_{60}$

**Experimental setup.** The sublimability of Li@$C_{60}$ was investigated by double sublimation thermal desorption spectroscopy (TDS). The material used for these experiments was charged as solution in $CS_2$ into small quartz or steel ovens and then deposited onto walls of the oven by drying. The ovens were further degassed under HV ($10^{-8}$ mbar) for at least 12 h at a temperature of 70 °C.

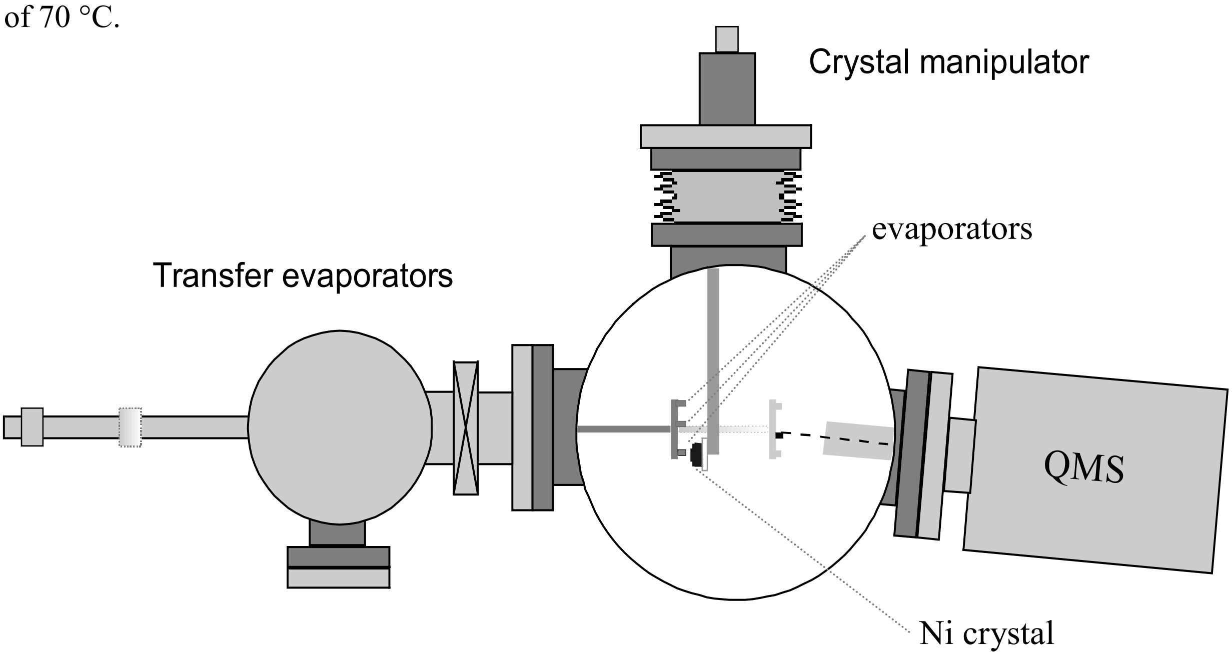

*Fig.3.4. Set-up for the double sublimation thermal desorption spectrometry*

A special setup with three ovens fixed on an UHV magnetically coupled sample transporter mounted in a load-lock chamber allowed us to manipulate these ovens inside the main UHV chamber and move them either directly in front of the mass spectrometer or in front of the Ni crystal for a film deposition (Fig.3.4). The ovens were placed in front of the Ni crystal only after reaching an oven temperature of 350 °C, in order to avoid the deposition of the residual solvent with the film.

The material was desorbed either directly from the oven (named hereafter “direct sublimation”) or from the Ni crystal (“double sublimation”) with a constant heating rate of 10 °C/s, up to 800 °C, and measured with a Balzers QMS 421 Quadrupole Mass Spectrometer. The neutral desorbed molecules reaching the QMS were ionised by electron impact, with an electron energy of 45 eV. At this electron energy there is a good balance between the ionisation efficiencies for $C_{60}$ and Li@$C_{60}$, on one side, and the low level of fragmentation of $C_{60}$ – indicated by the low $C_{58}$ ion signal in Fig.3.5 [KKT98, Kus98].

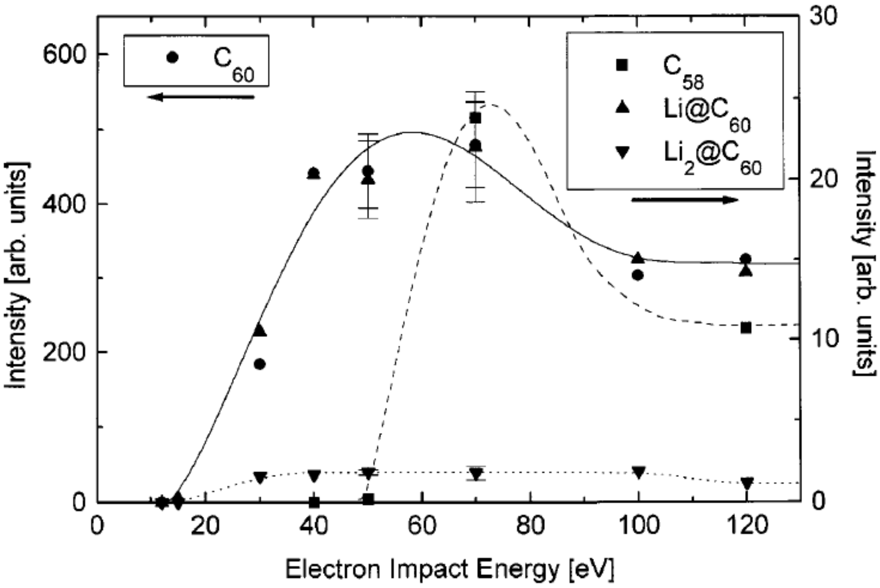

*Fig.3.5. Ion signals as a function of the electron energy in the ioniser of the quadrupole mass spectrometer, measured by Kusch et al. [KKT98, Kus98]*

**Thermal Desorption Spectroscopy Measurements.** Fig.3.6 shows the TDS signals obtained by direct desorption of the material from an oven degassed under high vacuum at 70 °C for 12 hours (a), and from an oven which was only kept under high vacuum at room temperature for 2 hours prior to the temperature-controlled desorption (b). The materials were still containing impurities like hydrocarbons after longer degassing, as can be seen in the low mass spectrum in Fig.3.7. Only the signals from the main solvents, oDCB (used in the HPLC purification process) and $CS_2$ (used for the preparation of the material), together with the Li@$C_{60}$ and $C_{58}$ signals, are shown in Fig.3.6.

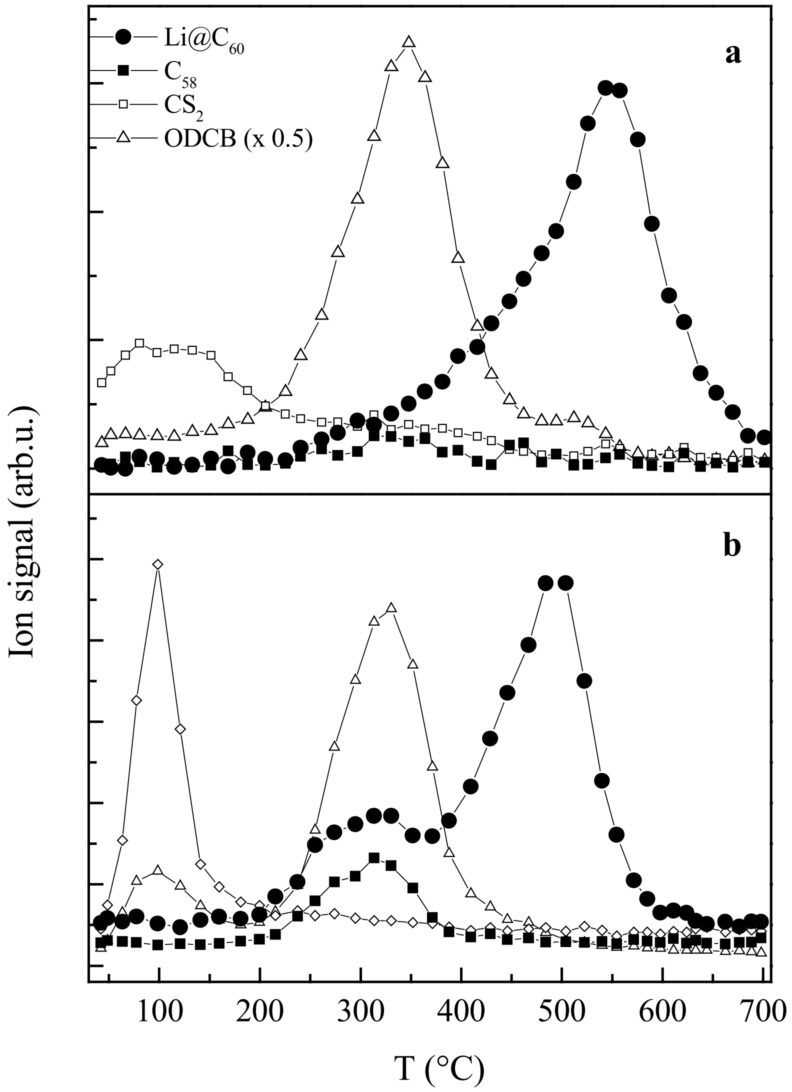

*Fig.3.6. Thermal desorption signals obtained by the direct desorption of the material: (a) from an oven degassed for 12 hours under high vacuum, at 50 °C, and (b) from an oven which was kept for 2 hours under high vacuum at room temperature prior to the temperature-controlled desorption.*

The $CS_2$ desorption threshold and maximum are at lower temperatures compared to the other masses recorded. The separation of the endohedral material from this solvent is straightforward. In the case of the not-degassed material, there is a high amount of Li@$C_{60}$ that desorbs at lower temperatures (with a peak at ~ 320 °C). This Li@$C_{60}$ may be carried by the desorbing oDCB solvent molecules, which show the peak at a similar temperature. This lower-temperature peak is much weaker for the long-degassed material than for the short-degassed material, although the relative content of oDCB is the same: $I_{oDCB}/ (I_{Li@C_{60}}+I_{C_{60}}+ I_{oDCB})$ = 13.8% for the degassed and 14% for the not degassed (the intensities need to be corrected for detection and ionisation efficiencies in order to calculate true ratios). We therefore conclude that the desorption of the endohedral molecules at these low temperatures is induced by other impurities than the residual solvents ($CS_2$ and oDCB), and these impurities are reduced by extended degassing.

It is important to note that the $C_{58}$ signal overlaps with this low-temperature Li@$C_{60}$ peak and decreases accordingly with the longer degassing times. The stronger Li@$C_{60}$ signal at ~ 500 °C is not accompanied by an enhanced $C_{58}$ signal. Since the low-mass impurities peak at lower temperatures, similar to the oDCB trace, we assume that this fragmentation is strongly activated by the impurities (other than solvent molecules), and most likely occurs in the ioniser of the mass spectrometer, as will be discussed in the following paragraph.

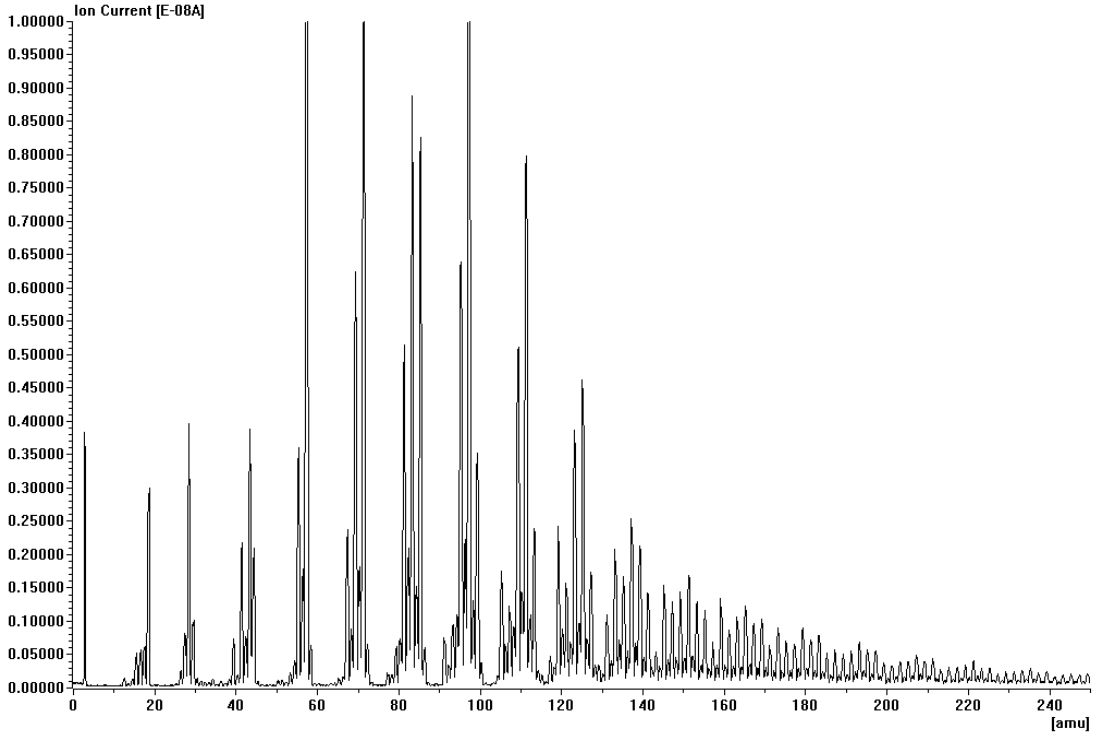

*Fig.3.7. Spectrum of lower masses from directly sublimed Li@$C_{60}$ material.*

The ratio $R = I_{Li@C_{60}} / (I_{Li@C_{60}} + I_{C_{60}})$ was evaluated from the TDS spectra, in order to analyse the fragmentation from Li@$C_{60}$ to $C_{60}$. A value of R = (9.2 ± 1.0)% was found for the sublimation directly from the evaporator. The double sublimation of films (first deposited on a Ni substrate) gave R = (9.8 ± 1.0) %, a good indication that the endohedral nature of the molecules is not lost through the fast sublimation. Laser Desorption Mass Spectrometry (LDMS) performed on films deposited by sublimation with a heating rate of 10 °C/s also confirms that the fast sublimation does not cause the decay of the endohedral molecules into $C_{60}$. A relative content of 95% Li@$C_{60}$ was obtained from the spectrum shown in Fig.3.8 and this value agrees with the estimate of the endohedral content found for the starting material from

HPLC analysis. The ratio found from the TDS spectra is, though, one order of magnitude lower than the ratio found from LDMS and HPLC analysis. The ionisation potential for Li@$C_{60}$ has been calculated to be 6.07 eV, 1.64 eV lower than for $C_{60}$ [BrE98] and their ionisation cross-sections are expected to be quite similar. We conclude that the Li@$C_{60}$ decays into $C_{60}$ due to the heating of the molecule by electron impact in the ioniser of the mass spectrometer.

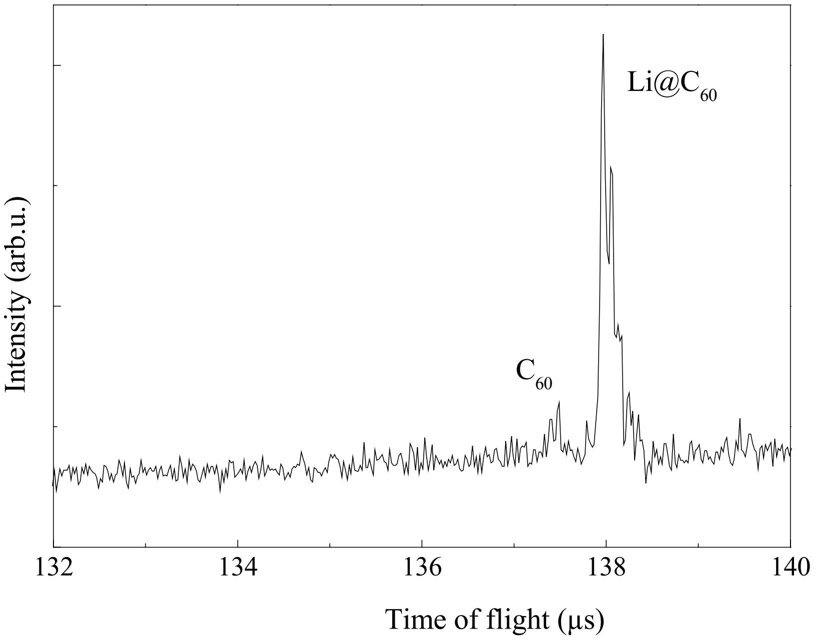

*Fig.3.8. Time of flight spectrum of positively charged ions produced by pulsed laser desorption/ionisation of a Li@$C_{60}$ film deposited with a heating rate of 10 °C/s.*

Despite the fragmentation of the Li@$C_{60}$ into $C_{60}$ in the ioniser of the QMS, we did not observe a Li ion signal in our spectra. The cross section for the electron impact ionisation for Li at 45 eV of ~ $3.2 \cdot 10^{-17}$ cm$^2$ [DBM99] is two orders of magnitude lower than for $C_{60}$ (~ $2.3 \cdot 10^{-15}$ cm$^2$ [VHS93]). While studying directly $Li^+$ irradiated $C_{60}$ films, with a $Li^+$:$C_{60}$ ratio of 1:1, Kusch et al. [KKT98] were observing a $Li^+$ signal by thermodesorption. Their samples were containing mainly intercalated Li atoms, as well as exohedral Li$C_{60}$, so that the desorbed Li ions are probably not due to eliberation from the $C_{60}$ cage by the electron impact excitation in the ioniser, but rather intercalated atoms.

The relative content of Li@$C_{60}$ in the unpurified films from Kusch et al. was found by TDS to be 4.6%, while the LDMS spectra gave a value of 6%. The TDS ratio was about half the ratio found in our measurements while the LDMS ratio was 16 times lower than the one found here for the purified material. For the present LDMS spectra, a $N_2$ laser at 337 nm was used, with a pulse width of 500 ps. In [KKT98], the LDMS measurements were performed using an excimer laser at 308 nm, with a pulse width of 10 ns. A stronger thermal destruction of the endohedral molecules can be expected from the laser desorption with the longer pulses, thus giving an underestimated content of endohedrals in the film. The films measured by Kusch et al. were not treated chemically for the purification and therefore were not containing solvent impurities. The amount of hydrocarbons was also lower than in our films. As we could see from Fig.3.6, the impurities are catalysing the destruction of Li@C$_{60}$ under electron impact. The endohedral ratio found from our TDS measurements can therefore be lowered by this effect.

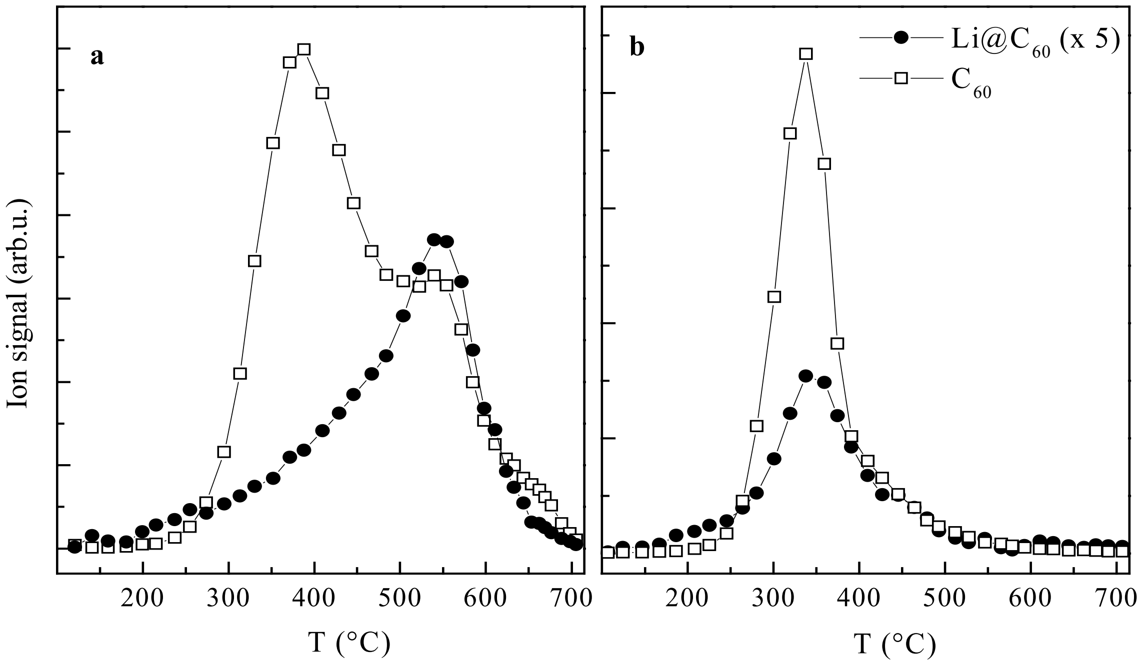

*Fig.3.9. C*$_{60}$ *and Li@C*$_{60}$ *thermal desorption signals from (a) direct sublimation from the oven (the same as in Fig.3.6a) and (b) sublimation of a film first vapour-deposited on the Ni substrate*

A comparison between the thermal desorption signals of C$_{60}$ and Li@C$_{60}$ obtained by (a) direct heating of the oven and by (b) heating a film deposited on Ni in front of the mass spectrometer is shown in Fig.3.9. When desorbed directly from a dried solution, the C$_{60}$ seems to have a double peak, one at lower temperatures (~380 °C) and another one, at about 550 °C, overlapping with the Li@C$_{60}$ peak. In the case of the double sublimation (i.e. desorption from the vapour deposited film), the Li@C$_{60}$ desorbs at lower temperatures (~ 340 °C), similar to the C$_{60}$ signal. The second peak in Fig.3.9a closely follows the Li@C$_{60}$ signal, so we can clearly relate it to the decomposition of the Li@C$_{60}$ under electron impact. The C$_{60}$ peak at lower temperature appears to be almost twice as strong as the peak at higher temperature. This strong C$_{60}$ peak can not be attributed to the residual C$_{60}$ from the material, since the ionisation cross-sections for $C_{60}$ and Li@$C_{60}$ are estimated to be very similar, and the starting material has a 95% nominal content of Li@$C_{60}$, which is preserved after sublimation according to LDMS. Therefore, both $C_{60}$ peaks should be linked to the desorption of Li@$C_{60}$, which probably has two chemically different states in solution, with different probabilities for losing the Li in the electron impact ionisation process. The impurities (oDCB solvent, water, hydrocarbons) desorb at lower temperatures and peak at ~ 350 °C, close to the first peak of $C_{60}$. We have already seen that these impurities, when present in higher amounts, catalyse the fragmentation of the $C_{60}$ cage and the loss of Li. We can assume that the first peak comes from the desorption of Li@$C_{60}$ molecules together with (or even attached to) impurities, leading to an efficient removal of the Li atoms from the $C_{60}$ cage through the excitation and ionisation by electron impact. The second peak, at higher temperatures (~ 540 °C), shows that part of the molecules have a higher binding energy in the film. We can assume that part of the Li@$C_{60}$ molecules bond in aggregates in solution. This seems to be in agreement with recent Raman spectroscopic measurements on films deposited by drying droplets of solutions on KBr substrates [CaG01], where the $A_g(2)$ pinching mode is shifted from 1469 $cm^{-1}$ (as found for $C_{60}$ monomers) to 1459 $cm^{-1}$, a value which is typically found for $C_{60}$ polymers. At this higher temperature of 540 °C the molecules are relatively free of impurities, which makes their destruction in the ioniser less efficient, thus explaining the higher Li@$C_{60}$ : $C_{60}$ ratio for the second peak. In the vapour-deposited films the molecules are not bound to each other, and therefore they desorb at a lower temperature, and peak at 340 °C. Since the ratio of endohedrals to empty fullerenes is only slightly higher for the double sublimation from the Ni crystal (9.8%) compared to the direct sublimation (9.2%), we have to conclude that the relative amount of (reactive) impurities is not significantly reduced by the deposition procedure employed in these experiments.

In conclusion, Li@$C_{60}$ is not decaying into $C_{60}$ during the fast sublimation. A thorough degassing of the material under vacuum at temperatures lower than 150 °C, prior to the vapour-deposition of thin films, is essential for avoiding the destruction of the cage in the presence of impurities. The comparison between the thermal desorption of the material dried from solution in the ovens and the desorption of the vapour-deposited films indicates that the molecules are bond in aggregates when dried from solution.

## 3.5 Optical properties of vapour-deposited Li@$C_{60}$ films

### 3.5.1 IR spectroscopy

The IR absorption spectra of droplet-dried films of purified Li@$C_{60}$ have been studied in the doctoral work of N. Krawez [Kra98]. Three main features have been largely discussed in this work. A broad absorption band between 400-500 $cm^{-1}$ was assigned to vibrational-rotational bands of $Li^+$, corresponding to a rattling motion of the ion within the cage [TKL96, Kra98]. A strong absorption peak at 1378 $cm^{-1}$ was assigned to the $F_{1u}(4)$ mode of the fullerene cage, softened by 51 $cm^{-1}$ compared to the empty $C_{60}$. The third feature, a strong peak at 1462 $cm^{-1}$, was correlated to the strongest Raman-allowed $A_g(2)$ “pentagonal pinching” mode in $C_{60}$. This vibrational mode could be both Raman and IR active, due to the breaking of the inversion symmetry of the Li@$C_{60}$ through the off-center position of the Li atom in the cage [LiT94, ToL95, AnC98].

The IR transmission spectrum of a vapour-deposited film of Li@$C_{60}$ is shown in Fig.3.10 (lower panel), together with the IR spectrum of a $C_{60}$ film deposited in a similar way (upper panel). Note that, in contrast to the IR spectra reported in [Kra98] for droplet-dried films, we found no significant difference between the IR absorption of vapour-deposited Li@$C_{60}$ and (Li@$C_{60}$)$_2$ films. The Li@$C_{60}$ spectrum is much richer compared to the IR spectrum of $C_{60}$, which consists of four three-fold degenerated first-order modes of $F_{1u}$ symmetry, at 526, 576, 1183 and 1429 $cm^{-1}$. These modes remain nearly unaffected in frequency in Li@$C_{60}$. The $F_{1u}(4)$ mode at 1429 $cm^{-1}$ is, in the figure, covered under the envelope of the broad absorption at 1462 $cm^{-1}$. The two most prominent lines in the spectra are at 1377 and 1462 $cm^{-1}$, similar to the droplet-dried films. The interpretation that is given here for the peak at 1462 $cm^{-1}$ is different from the interpretation of Krawez in [Kra98]. Raman spectra of droplet-dried films showed the $A_g(2)$ mode at 1459 $cm^{-1}$, while for vapour-deposited films it is at 1467 $cm^{-1}$ [CaG01]. In the IR spectra this peak is always measured at 1462 $cm^{-1}$. Therefore, we conclude that this IR mode is not correlated to the $A_g(2)$ Raman mode of the fullerene. The degeneracy of the $F_{1u}(4)$ mode may be lifted through the endohedral doping, leading to a splitting of this mode into three lines at 1377, 1429 and 1462 $cm^{-1}$. The intensities of these $F_{1u}(4)$ modes are strongly enhanced compared to the other $F_{1u}$ modes due to the charge transfer from the encapsulated Li atom to the fullerene cage. This leads to an electron-molecular-vibration coupling, where vibrational modes of molecular $C_{60}$ acquire electronic oscillator strength via coupling to virtual electronic transitions between the $C_{60}$ $t_{1u}$ (partially occupied by the 2p electron of Li) and $t_{1g}$ molecular orbitals [RiC92]. This effect was first observed for the $F_{1u}(2)$ and $F_{1u}(4)$ modes in $A_xC_{60}$ (A = Rb, K, x = 1 ÷ 6) [MKM94, DDE96]. The strength of this coupling depends on the dopant concentration x, i.e. on the total number of electrons donated to the fullerene cage.

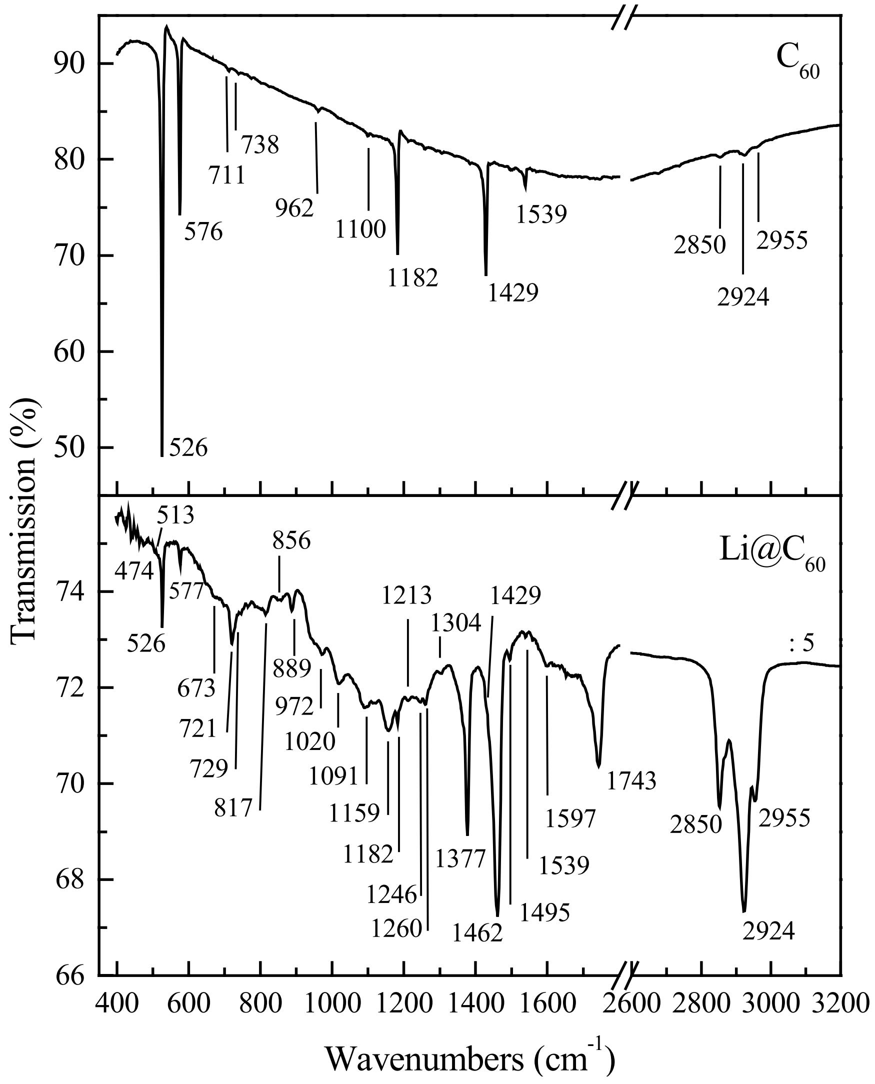

*Fig.3.10. IR transmission spectrum of a vapour-deposited Li@$C_{60}$ film. The IR spectrum of a $C_{60}$ film is shown, for a comparison, in the upper graph.*

Andreoni and Curioni [AnC98] have calculated the IR spectrum of the endohedral Li@$C_{60}$ and the exohedral Li$C_{60}$ (both shown in Fig.3.11), based on an ab initio approach within density-functional-theory. A total charge transfer from the Li atom to the $C_{60}$ cage was assumed for the Li@$C_{60}$ molecule. The frequencies and relative intensities of the peaks in the calculated and the measured spectra are listed in Table 3.1. The peaks from droplet-dried films of Li@$C_{60}$ reported by Krawez [Kra98] and the modes of empty $C_{60}$ (from [DDE96]) are also listed in the table.

There is a good qualitative agreement between the theoretical and experimental peaks in Li@$C_{60}$.

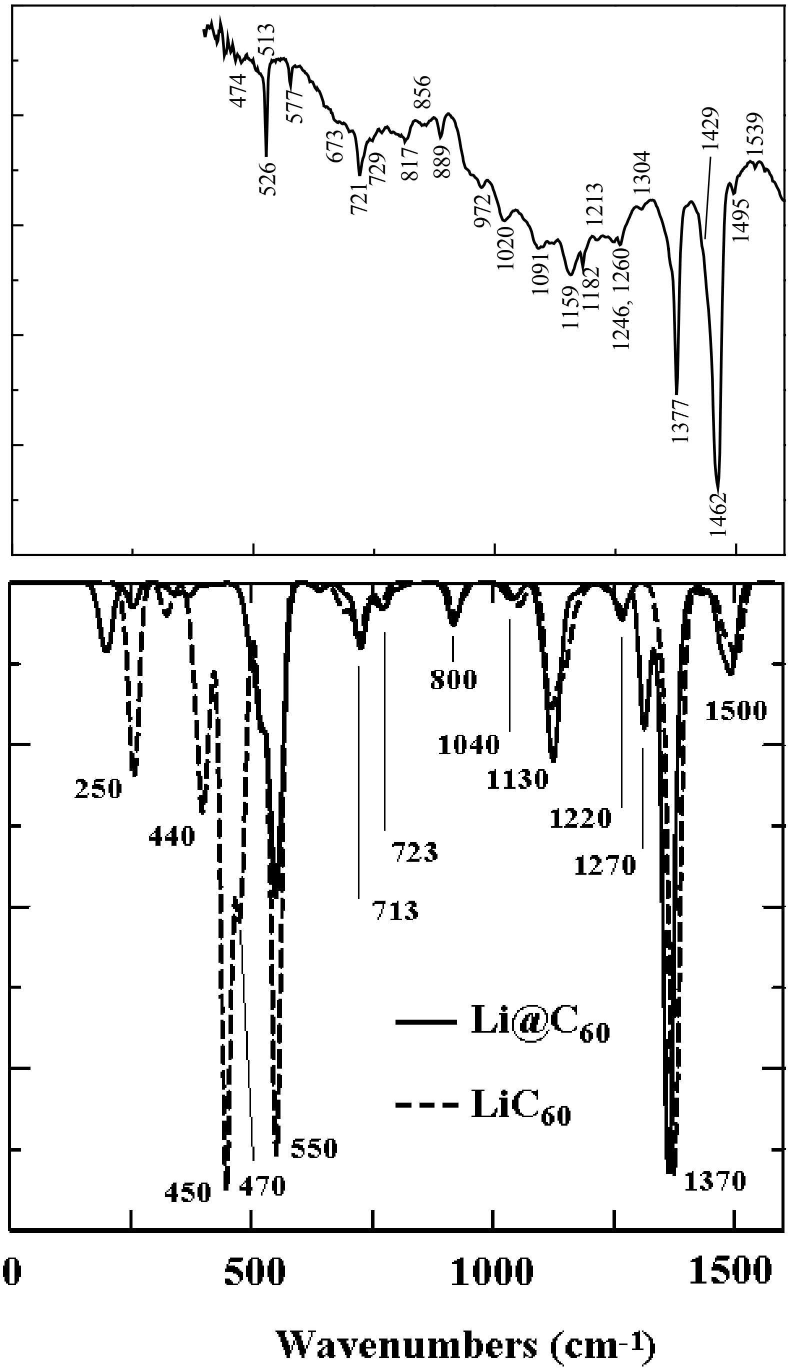

*Fig.3.11. Calculated infrared spectra of Li@$C_{60}$ and exohedral Li$C_{60}$ [AnC98, CaG01]. The corresponding section of the experimental transmission spectrum from Fig.3.10 is shown for comparison in the upper graph.*

According to the calculations, the exohedral Li$C_{60}$ compound should show a series of strongly activated IR modes, at ~440, 450 and 470 cm$^{-1}$. Krawez et al. [TKL96, Kra98] assigned two broad absorptions at 445 and 484 cm$^{-1}$ to vibrational-rotational absorptions of the Li ion inside the cage. These absorptions were measured in Li$^+$-irradiated films of C$_{60}$ and, with much weaker intensity, in droplet-dried films of purified Li@C$_{60}$. No absorption is found in this spectral range from films of vapour-deposited Li@C$_{60}$, except for a very weak feature at ~ 474 cm$^{-1}$. It is attempting to assign the broad absorptions at 400-500 cm$^{-1}$ to exohedral species of LiC$_{60}$, which might form in the droplet-dried films due to the higher amounts of impurities. Polymerised Li@C$_{60}$ is also present in the Li$^+$-irradiated films of C$_{60}$ (reducing the solubility at higher ion doses). The TDS measurements discussed above suggest that the molecules bond in aggregates in the dried material. The absorption at 400-500 cm$^{-1}$ can be attributed to polymeric modes of Li@C$_{60}$. The molecules do not organise in aggregates in the vapour-deposited films, where these modes are not observed anymore. Two modes at 474 and 484 cm$^{-1}$ are indeed induced by photopolymerisation of the vapour-deposited films (see Fig.3.29 and the discussion in Section 3.7.2).

A relatively strong absorption peak can be observed in Fig.3.10 at 1743 cm$^{-1}$. The IR spectra from endohedrally and exohedrally doped C$_{60}$ are discussed in the literature for frequencies of up to 1500 cm$^{-1}$, both in theoretical and experimental studies. It is therefore difficult to give a clear assignment of this peak. C=O groups are known to have absorption bands at 1730 and 1785 cm$^{-1}$ [WWH96]. The band at 1730 cm$^{-1}$ is close to the one observed in our spectra, but we never observe the second band at ~ 1785 cm$^{-1}$, which would have a similar intensity. We believe that the peak at 1743 cm$^{-1}$ corresponds to an IR mode of the Li@C$_{60}$ molecule rather than to oxygenated species in the film. However, the presence of oxygenated carbon groups in the films can not be excluded. The broad background at ~ 1100 cm$^{-1}$ can be associated to C-O groups [WWH96]. Its magnitude varies in different samples in a similar way as the magnitude of the strong peaks at 2850, 2924 and 2955 cm$^{-1}$, which correspond to absorptions of aliphatic hydrocarbon molecules. This indicates the presence of oxygenated aliphatic hydrocarbon impurities in the films. The relative concentration of these impurities can not be estimated from these measurements, since the absorption coefficients for Li@C$_{60}$ are not known. Nevertheless, Li@C$_{60}$ is a large molecule with high symmetry and, similar to C$_{60}$, a poor IR absorber. Small amounts of IR-active hydrocarbon molecules could easily account for these strong lines in the spectra. TDS measurements have shown that the hydrocarbons desorb at lower temperatures than the Li@C$_{60}$ molecules (see Section 3.4.2). We can therefore expect a phase separation between these molecules, with the Li@C$_{60}$ film deposited on “buffer” layer formed by the hydrocarbons.

| Li@$C_{60}$ present exp.[a] | Li@$C_{60}$ theory [AnC98][b] | Li$C_{60}$ theory [AnC98][b] | Li@$C_{60}$ exp. [Kra98][c] | $C_{60}$ exp. [DDE96][d] |
|---|---|---|---|---|
| | | 440 (m) | | |
| | | 450 (s) | | |
| 474 (w) | | 470 (s) | 400-500 (s) | |
| 513 (w) | | | | |
| 526 (m) | | | 527 (s) | 526 (s) |
| 577 (m) | 550 (s) | 550 (s) | 570 (s) | 576 (s) |
| 673 (w) | | | | 674 (w)* |
| 721 (m) | 713 (m) | 713 (m) | | 712 (w)* |
| 729 (w) | 723 (w) | 723 (w) | | |
| 817 (m) | 800 (w) | 800 (w) | ~ 800 (m) | |
| 856 (w) | | | | |
| 889 (m) | | | | |
| 972 (m) | | | | 962 (w)* |
| 1020 (m) | 1040 (w) | 1040 (w) | | 1016 (w)* |
| 1091 (m) | | | | 1100 (w)* |
| 1159 (m) | 1130 (m) | 1130 (m) | | 1164 (w)* |
| 1182 (w) | | | | 1183 (s) |
| 1213 (w) | 1220 (w) | 1220 (w) | | 1213 (w)* |
| 1246 (w) | | | | 1242 (w)* |
| 1260 (w) | 1270 (m) | | 1258 (m) | 1259 (w)* |
| 1377 (s) | 1370 (s) | 1370 (s) | 1378 (s) | |
| 1429 (w) | | | | 1429 (s) |
| 1462 (s) | | | 1462 (s) | |
| 1495 (w) | 1500 (m) | 1500 (m) | | 1496 (w)* |
| 1539 (w) | | | | 1539 (m)* |
| 1597 (w) | | | | |
| 1743 (s) | | | | 1746 (w)* |

*Table 3.1. Li@$C_{60}$ IR modes (cm$^{-1}$) obtained in this experiment (a), compared with the IR modes calculated by Andreoni and Curioni [AnC98] for endohedral Li@$C_{60}$ and exohedral Li$C_{60}$ (b), with the experimental peaks reported by Krawez [Kra98] for droplet-dried films of Li@$C_{60}$ and with $C_{60}$ peaks [DDE96]. Combination modes from $C_{60}$ are marked with a star. The intensities are given in parenthesis: w, m and s denote weak, medium and strong, respectively.*

## 3.5.2 UV-VIS spectroscopy

### UV-VIS absorption and the electronic structure of $C_{60}$.

$C_{60}$ is an almost ideal molecular solid, with weak Van der Waals interactions between the molecules. The absorption spectrum of solid $C_{60}$ (shown in Fig.3.12) is very similar to the corresponding spectrum of $C_{60}$ in solutions. The strong absorption bands at higher energies can be well interpreted using the molecular states of the isolated molecule. The four strong optical absorption bands in Fig.3.12 are identified with the dipole-allowed transitions (within the single electron level diagram of molecular $C_{60}$ – see Fig.3.13) $h_u \rightarrow t_{1g}$ (2.7 eV), $h_g + g_g \rightarrow t_{1u}$ (3.6 eV), $h_u \rightarrow h_g$ (4.6 eV) and $h_g + g_g \rightarrow t_{2u}$ (5.6 eV). The peaks are slightly red-shifted in energy and considerably broadened, compared to the absorption in solution. The downshift of the spectrum is introduced by the lattice potential [DDE96]. The broadening of the peaks can be explained by the broadening of the molecular orbitals into electronic energy bands, with widths of the order of 0.5 to 1.0 eV [DDE96, XuS94]. Grain boundary defects in the (generally) polycrystalline $C_{60}$ films can also lead to the broadening of the absorption, by lowering the local symmetry of $C_{60}$ and lifting the high degeneracy of the intramolecular modes involved in vibronic transitions [DDE96].

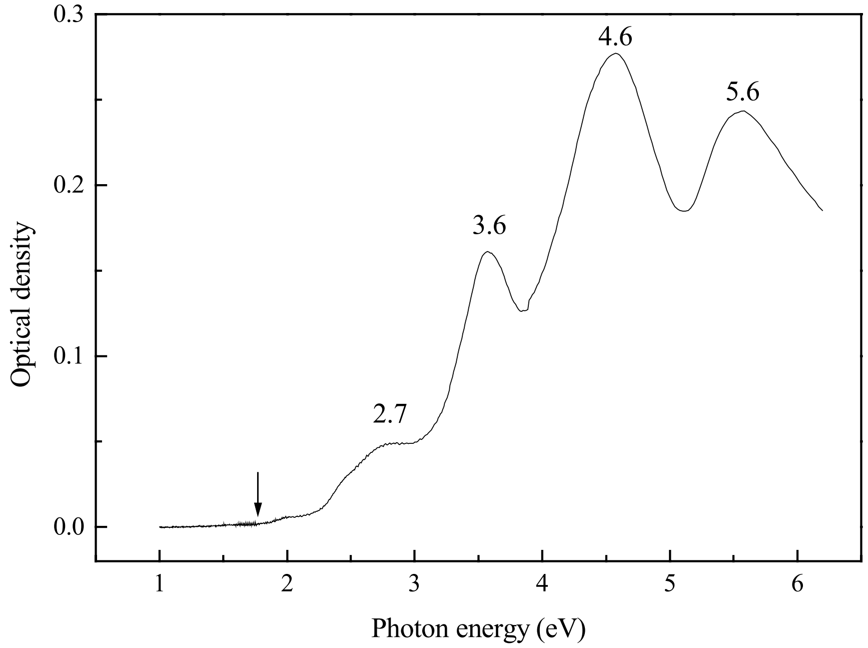

*Fig.3.12. Absorption spectrum from a 10 ML $C_{60}$ film. The arrow marks the onset of absorption, at ~ 1.75 eV.*

The differences between the absorption in solution and in solid state become more important in the low-energy range of the spectrum. The intensities of the bands at 2.7 and 3.6 eV, relative to the higher bands at 4.6 and 5.6 eV, are significantly higher in the solid phase. A broad and fairly intense shoulder appears at the lower energy side of the absorption at 2.7 eV. Tsubo and Nasu [TsN94] have calculated that the excitations in solid $C_{60}$ at energies 2.33 eV and higher correspond to the formation of charge transfer excitons. Kazaoui et al. [KMT98] have assigned the most significant charge transfer states at 2.43 and 3.5 eV, based on electroabsorption and luminescence experiments. The coupling of the CT state at 2.43 eV to the Frenkel excitonic state at 2.7 eV leads to a stronger activation of this state and an enhancement of the absorption at 2.7 eV.

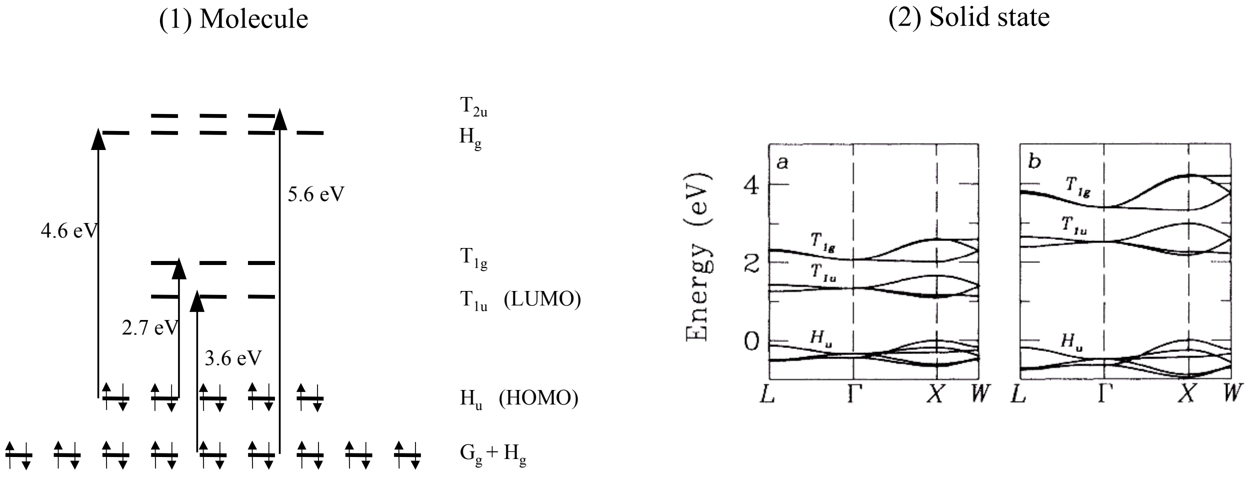
(1) Molecule

(2) Solid state

*Fig.3.13. (1) Single electron level diagram for the isolated $C_{60}$ molecule. The electric dipole allowed transitions shown by arrows correspond to the absorption bands marked in Fig.3.12. (2) Calculated HOMO ($H_u$), LUMO ($T_{1u}$) and LUMO+1 ($T_{1g}$) for the fcc solid $C_{60}$ : (a) local density approximation and (b) quasiparticle approach [ShL93].*

The onset of the optical absorption in $C_{60}$ films is found at ~ 1.7 eV (marked with an arrow in Fig.3.12). Optical transitions between the HOMO ($H_u$) and the LUMO ($T_{1u}$) molecular levels are optically forbidden within the one-electron picture of an isolated molecule. A symmetry breaking mechanism for this molecular optical selection rule is required to activate these optical transitions. The vibronic coupling between excited electronic states and vibrational states (Herzberg-Teller effect) can account for the weak absorption at 1.7 eV [DDE96]. In this energy range, the excitations are localised on a single molecule to form Frenkel excitons, according to the calculations of Tsubo and Nasu [TsN94]. Early band calculations found a band gap for $C_{60}$ of ~ 1.5 eV, close to this onset in the optical absorption and in good agreement with the lowest peak in electron energy loss spectra [DDE96]. The experimental bandgap between HUMO and LUMO band states has been inferred to be around 2.3-2.6 eV from direct and inverse photoemission [LVK92, TSM92]. Shirley and Louie calculated, using a quasiparticle approach, a direct bandgap of 2.15 eV for the fcc solid $C_{60}$ [ShL93] (see also Fig.3.13). Orientational disorder removes sharp features in the density of states but yields negligible changes in the band edges and the bandwidths (of ~ 1 eV).

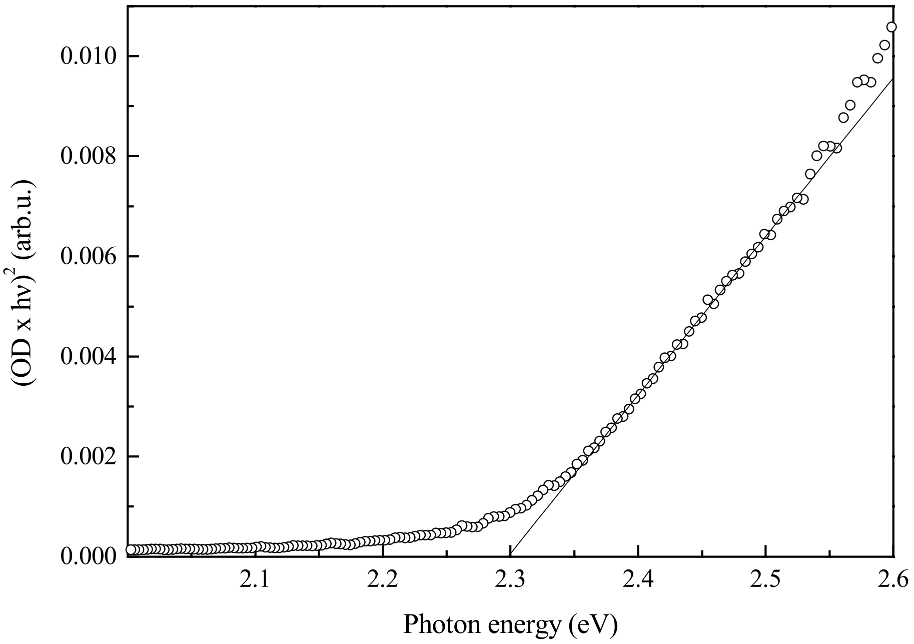

*Fig.3.14. Plot of (OD x $h\nu$)$^2$ versus photon energy for a 10 ML film of $C_{60}$. Least-squares fit for the low-energy linear region yields an energy intercept of $E_g = (2.3 \pm 0.1)$ eV.*

The low energy part of the optical absorption spectrum can be analysed according to the well-known expression of the absorption coefficient derived for the fundamental absorption in semiconductors [Abe72]:

$$\alpha \sim (h\nu)^{-1} \cdot (h\nu - E_g)^{n/2}\,, \tag{3.2}$$

where n depends on whether the transition is direct (n = 1) or indirect (n = 4). The optical density is proportional to the absorption coefficient: $OD \sim \alpha \cdot d$, where $d$ is the thickness of the film. A plot of $(OD \text{ x } h\nu)^{1/2}$ versus $h\nu$ does not lead to any straight lines over any part of the low-energy spectrum. The plot of $(OD \text{ x } h\nu)^2$ versus $h\nu$ is shown in Fig.3.14. We can evaluate a direct-bandgap energy of (2.3 ± 0.1) eV from the x-axis intercept at the extrapolated straight line fitted to the linear part of the spectrum. This result is in good agreement with the photoemission experiments and with the theoretical prediction for the type and the energy of the bandgap.

### UV-VIS absorption of Li@C$_{60}$ and (Li@C$_{60}$)$_2$.

The UV-VIS absorption spectra from Li@C$_{60}$ and (Li@C$_{60}$)$_2$ films vapour-deposited on quartz substrates is shown in Fig.3.15, together with the absorption spectrum of a C$_{60}$ film shown here for a qualitative comparison.

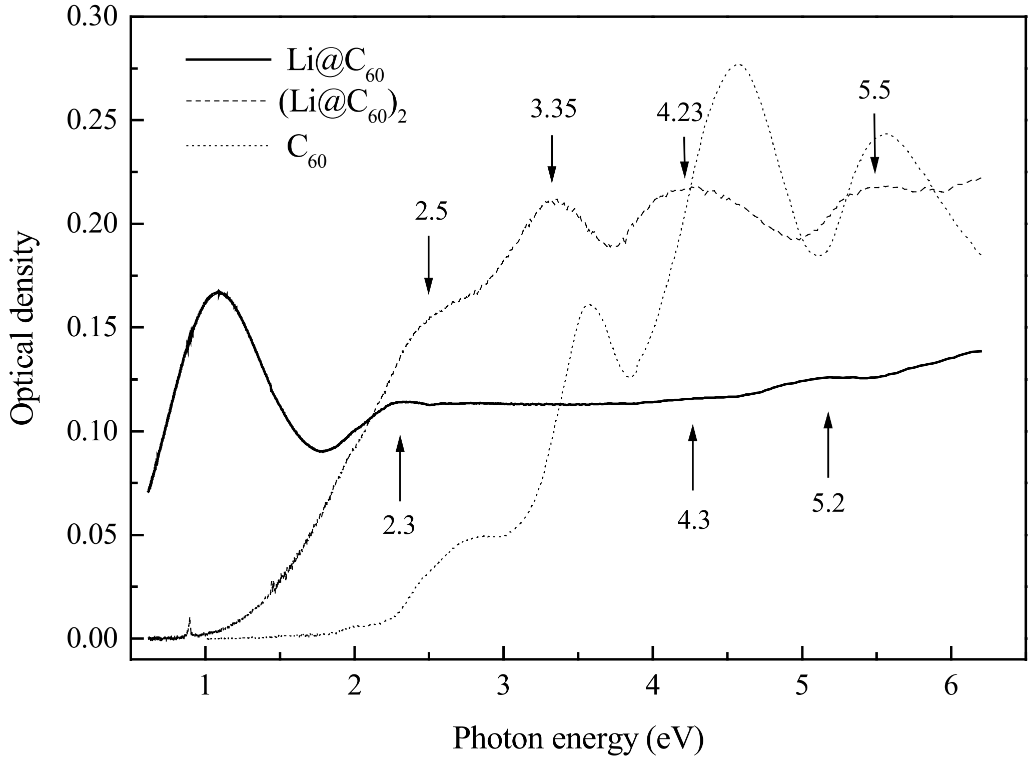

*Fig.3.15. UV-VIS absorption from thin films of Li@C$_{60}$ (solid line), (Li@C$_{60}$)$_2$ (dashed line) and C$_{60}$ (dotted line). The spectra are scaled for a better comparison. The absorption peaks in Li@C$_{60}$ and (Li@C$_{60}$)$_2$ are marked in the lower and upper part of the figure, respectively. The weak peak at 0.9 eV is due to absorption in the quartz substrate.*

The main feature in the spectrum of Li@C$_{60}$ is a strong absorption band centered at 1.1 eV. A weak absorption at 1.15 eV was also measured from C$_{60}^-$ anions in solutions [DDE96] and in thin films [KAT95]. This absorption is attributed to a transition between the $t_{1u}$ (LUMO) – $t_{1g}$ (LUMO+1) levels (in the single-electron level picture for C$_{60}$) and is considered as clear evidence for the electron transfer from the Li atom to the $t_{1u}$ (LUMO) level of the fullerene cage. The absorptions specific to the C$_{60}$ are very weak and shifted to lower energies: the $h_u \rightarrow t_{1g}$ transition is shifted from 2.7 eV to 2.3 eV, the $h_u \rightarrow h_g$ transition from 4.6 eV to 4.3 eV and the $h_g + g_g \rightarrow t_{2u}$ transition from 5.6 eV to 5.2 eV. The transition at 3.6 eV, involving the $t_{1u}$ level ($h_g + g_g \rightarrow t_{1u}$), is not seen in Li@C$_{60}$.

The spectrum of the (Li@C$_{60}$)$_2$ film is qualitatively closer to the spectrum of the C$_{60}$ film. The absorptions are weaker, broadened and red-shifted compared to C$_{60}$. It is important to note that these absorptions are not red-shifted in solutions of Li@C$_{60}$ and (Li@C$_{60}$)$_2$ compared to solutions of C$_{60}$ [Kra98]. The red shift and the broadening of the peaks in the solid state indicate a stronger molecular interaction resulting in a larger delocalisation of the electronic states for the solid endohedral material.

The absorption peak at 1.1 eV is only seen in the spectrum of vapour-deposited Li@C$_{60}$. The deposition conditions dramatically affect the intensity and the energy of this peak. The Li@C$_{60}$ films are normally deposited by heating the material in the oven within 30 s to a temperature of 380-385 °C. The $t_{1u} - t_{1g}$ absorption band shifts at higher energies by ~ 0.25 eV for films deposited at a slightly higher temperature, of 395 °C. A blue shift of ~ 0.9 eV and a decrease in the intensity of this absorption band were also observed for films deposited at 385 °C on a substrate heated at 150 °C and annealed for 5 minutes. We conclude that this effect can not be attributed to a different ordering of the molecules in the solid state, due to differences in the deposition rate and / or different mobility on the substrate. A possible chemical transformation by thermal interactions of the molecules play a crucial role for their solid-state properties. The nature of these interactions is not known yet.

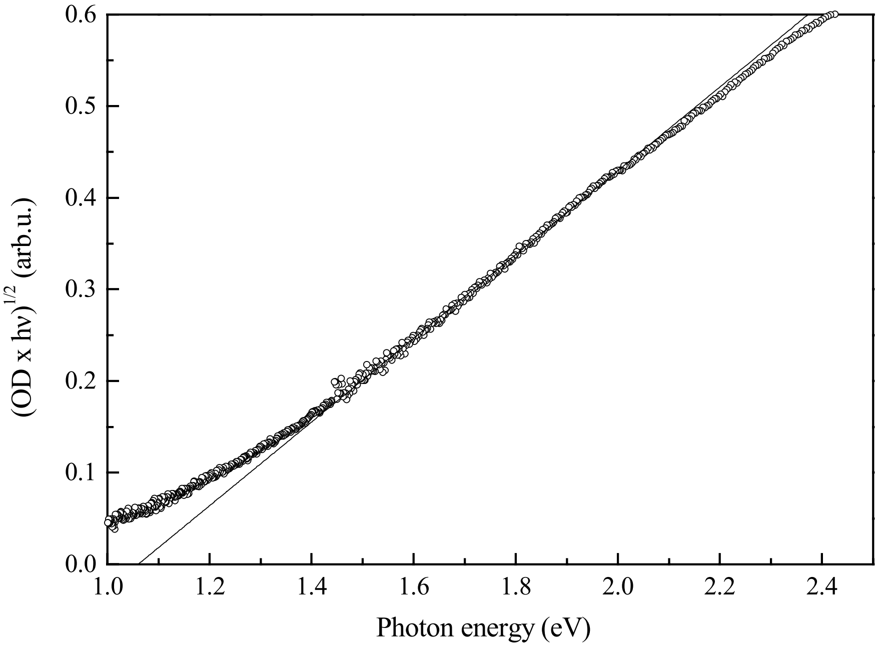

*Fig.3.16. Plot of (OD x hν)$^{1/2}$ versus photon energy for a film of (Li@C$_{60}$)$_2$. Least-squares linear fit for the low-energy linear region yields an energy intercept of $E_g = (1.06 \pm 0.1)$ eV.*

The spectra from solutions, as well as from the vapour-deposited (Li@C$_{60}$)$_2$ film, do not show an absorption peak in the near-IR energy region. Having in view the tendency of Li@C$_{60}$

to cluster in/from solutions, evidenced in the TDS measurements discussed in Section 3.4.2, we attribute the absorption at 1.1 eV to the monomeric state of Li@$C_{60}$, which is obtained only after the vapour-deposition of this molecule. In (Li@$C_{60}$)$_2$, both $Li^+$ cations inside the cages are expected to get closer to the intermolecular bond, inducing a localisation of the extra-charges from the fullerenes around this bond [CaG01]. This localisation of the charges could lead to an electronic structure similar to that of the neutral $C_{60}$.

The fundamental absorption edge for Li@$C_{60}$ can not be seen in this spectral range. An absorption onset at ~ 600 $cm^{-1}$ (0.075 eV) can be inferred from the IR absorption spectra (see also [Kra98]). The absorption onset in the (Li@$C_{60}$)$_2$ film appears at 0.8 eV. The low-energy part of this spectrum was analysed using equation (3.2). A plot of $(OD \text{ x } h\nu)^2$ versus $h\nu$, characteristic to a direct band gap, does not give any straight lines in this energy range. The $(OD \text{ x } h\nu)^{1/2}$ versus $h\nu$ curve shown in Fig.3.16 shows an extended linear range, characteristic for an indirect-bandgap. By fitting this linear part of the curve to a straight line we find, from the x-axis intercept of this line, an energy of (1.06 ± 0.1) eV for the indirect-bandgap in (Li@$C_{60}$)$_2$.

## 3.6 Excitation dynamics

### 3.6.1 Experimental setup

The relaxation dynamics in $C_{60}$, Li@$C_{60}$ and (Li@$C_{60}$)$_2$ thin films after excitation with photons of 2 eV energy, was measured using a standard two-colours pump-probe technique. A Cr:forsterite laser (oscillator and regenerative amplifier) was used to generate 155 fs pulses of ~ 100 μJ at 1250 nm, with a repetition rate of 1 kHz. The second harmonic of the laser radiation at 625 nm, generated in a LBO crystal, was used as a pump beam. The fundamental beam at 1250 nm was used as the probe. The experimental setup is shown in Fig.3.17. Two lenses of 20 cm focal length were used to focus the beams on the sample. The diameter of the pump beam was 320 μm, while the probe beam was focused to 240 μm. The intensity of the probe on the sample was about ten times lower than the intensity of the pump. The transient change of the transmittance at 1250 nm was measured using lock-in technique. The pump beam was chopped at ~ 240 Hz to generate a reference frequency. The pump and probe beams were incident on the sample at slightly different angles (by about 3°), to ensure a spatial separation of the beams in front of the Ge-photodiode used to detect the 1250 nm beam. A RG850 filter was blocking any scattered light at 625 nm. A half-wave plate – polariser combination was used to vary the intensity of the pump beam on the sample. No time-dependent change was detected from a clean quartz window, showing that the substrate does not contribute to the dynamics observed from the films.

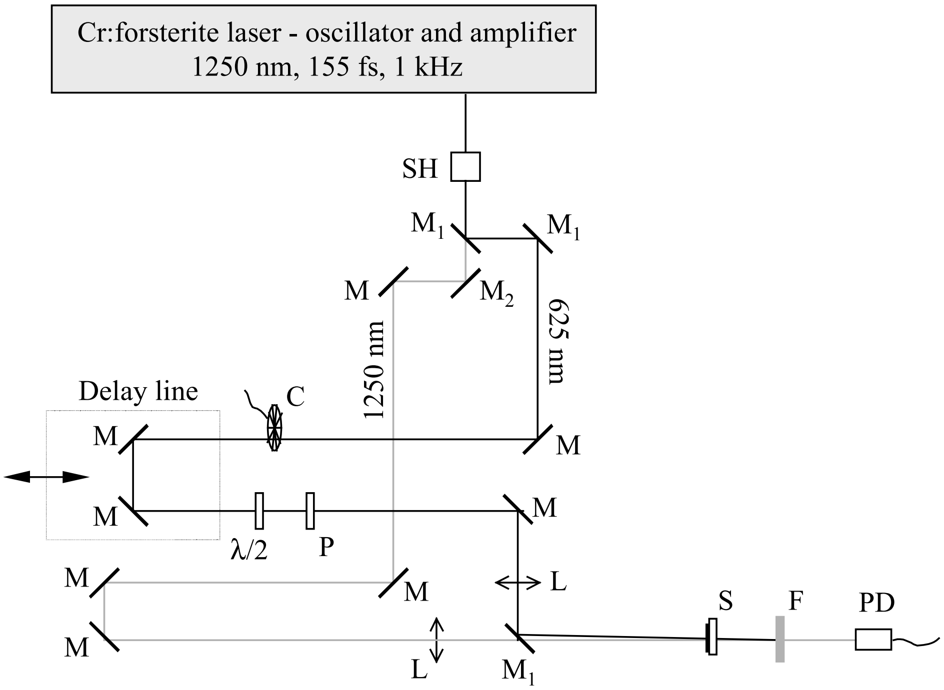

*Fig.3.17. Experimental setup: SH: LBO crystal for the generation of the second harmonic; M: Al- mirror; $M_1$: dielectric mirror for 625 nm; $M_2$: dielectric mirror for 1250 nm; λ/2: half-wave plate; P: polariser; C: chopper; L: lens of 20 cm focal length; S: sample; F: RG850 filter; PD: Ge-photodiode.*

Thin films of $C_{60}$, Li@$C_{60}$ and (Li@$C_{60}$)$_2$ were deposited by sublimation on quartz substrates. The structure of the films was checked with atomic force microscopy (AFM). Li@$C_{60}$ organises in islands of ~ 3 µm diameter and a thickness of ~ 1.15 µm, with an average coverage of 60% (Fig.3.18a). The film absorbs 50% of the pump beam at 625 nm.

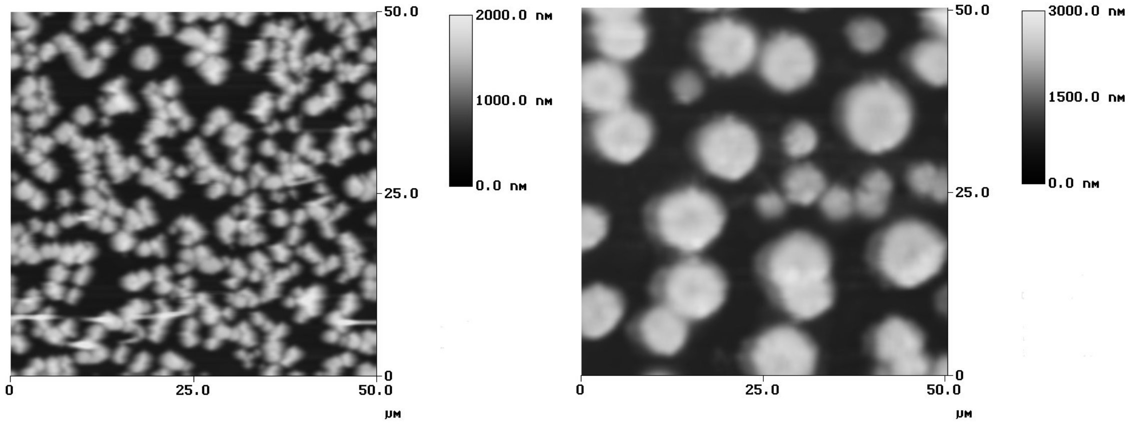

(a) (b)

*Fig.3.18. Topography of the endohedral films measured by AFM: (a) Li@$C_{60}$ and (b) (Li@$C_{60}$)$_2$*

$(Li@C_{60})_2$ forms islands of ~ 9 μm diameter with a thickness of ~ 1.5 μm and a coverage of ~ 55% (Fig.3.18b). The absorption of this film at 625 nm wavelength was 60%. The $C_{60}$ films show a rather uniform coverage of the surface. The thickness of the film chosen here for comparison was 1.05 μm, having an absorption of 70% at the pump wavelength of 625 nm. The excitation density generated by the same incident fluence of the pump beam is similar in all three samples.

### 3.6.2 Energetics

Fig.3.19 shows transient differential transmission traces from the Li@$C_{60}$ (a), $(Li@C_{60})_2$ (b) and $C_{60}$ (c) films, for an incident pump fluence of 7.75 mJ/cm$^2$. The negative signal obtained for $C_{60}$ and $(Li@C_{60})_2$ corresponds to an induced absorption as a result of the photoexcitation. For Li@$C_{60}$ the signal shows a transient bleaching of the absorption at 1250 nm.

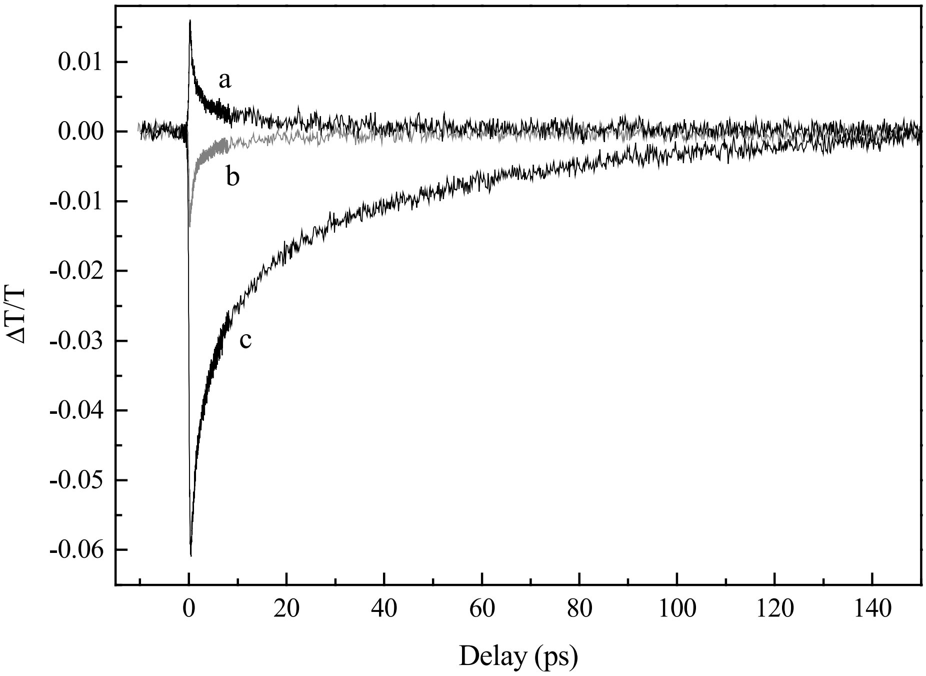

*Fig.3.19. Transient differential transmission at 1250 nm following the photoexcitation of (a) Li@$C_{60}$, (b) $(Li@C_{60})_2$ and (c) $C_{60}$ films at 625 nm with 7.75 mJ/cm$^2$.*

The different behaviour for $C_{60}$ and Li@$C_{60}$ can be understood based on the density of states of the molecules calculated by Broclawik and Eilmes [BrE98], schematically shown in Fig.3.20. The electronic structures were calculated by means of density functional methodology. The density of states (DOS) of the Li@$C_{60}$ molecule closely resembles the DOS of $C_{60}$, with the Fermi level shifted upwards and a weak contribution from Li 2s to the total DOS above the Fermi level. However, the shift of the Fermi level appears to be underestimated in these calculations. The three-fold degenerated $t_{1u}$ level of the endohedral fullerene is partially occupied due to the intramolecular charge transfer, as seen from the ground-state UV-VIS absorption of the Li@$C_{60}$ films (see Fig.3.15). The oblique lines in Fig.3.20 indicate occupied states. The transitions relevant for the two-colours pump-probe scheme used in the present measurements are shown in the figure.

In the case of $C_{60}$ there is no ground-state absorption at the probe photon energy of 1 eV. The excitation with 2 eV induces a vibronically-coupled transition from the $h_u$ (HOMO) to the $t_{1u}$ (LUMO) level (see also Section 3.5.2). The separation between $t_{1u}$ and $t_{1g}$ levels is ~ 1.1 eV, and the optical transition between these two levels is dipole-allowed. Therefore, the excited molecules will absorb the probe photons at 1 eV, giving rise to a transient induced absorption, which was measured as a negative differential transmission trace in Fig.3.19.

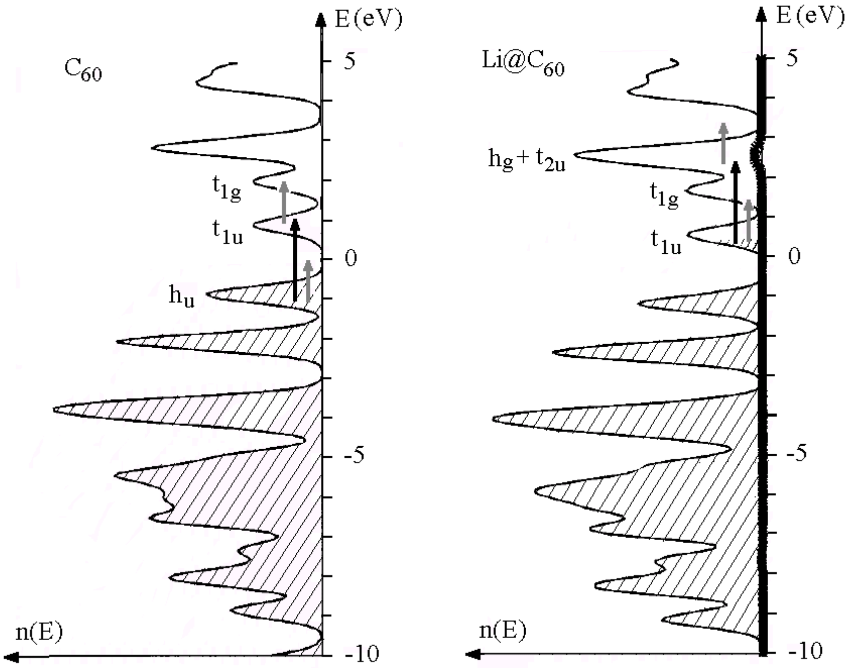

*Fig.3.20. Schematic of the density of states for $C_{60}$ and Li@$C_{60}$, after [BrE98]. The partial contribution of the enclosed Li metal in Li@$C_{60}$ is marked with a thick line. The transitions corresponding to the photon energy of the pump (2 eV) are marked with black arrows and transitions corresponding to the probe (1 eV) are marked with grey arrows. The symmetries of the levels involved in these transitions are also noted figure.*

The $t_{1u}$ level of the fullerene cage in Li@$C_{60}$ is partially occupied via the intramolecular charge transfer from the Li 2s orbital, as discussed in Sections 3.3.2 and 3.5.2. Li@$C_{60}$ has a relatively strong ground state absorption centered at 1.1 eV, close to the probe photon energy of 1 eV. The excitation with 2 eV induces a transition from the $t_{1u}$ level to the $h_g + t_{2u}$ levels. No absorption at 1 eV can occur from these levels, as indicated in Fig.3.20, thus determining the absorption bleaching or positive differential transmission trace in Fig.3.19. Within this simple picture, the amplitude of the transient change should be similar to the amplitude of the change in the C$_{60}$ film, which is not the case. Absorption at 2 eV can also occur from the $h_u$ level to the partially occupied $t_{1u}$ level, which would generate a transient absorption trace rather than bleaching. However, the absorption cross-section for the dipole-allowed $t_{1u} \rightarrow h_g + t_{2u}$ transition is expected to be higher than the cross-section for the weak vibronically-coupled $h_u \rightarrow t_{1u}$ transition, and the signal is dominated by the bleaching of the absorption. On the other hand, the density of states in Fig.3.20 is calculated for single Li@C$_{60}$ molecules. Strong intermolecular interactions in the solid state can determine the broadening of these levels, thus providing accessible higher-lying electronic states for the absorption at 1 eV from the excited $h_g + t_{2u}$ levels.

No DOS calculations are available for (Li@C$_{60}$)$_2$. We can intuitively give the same explanation as for the C$_{60}$ for the induced absorption observed from (Li@C$_{60}$)$_2$ films because of a fairly similar ground-state absorption spectrum (see Fig. 3.15 in chapter 3.5.2). However, the probe photon energy of 1 eV is above the onset of absorption in (Li@C$_{60}$)$_2$ films (at 0.8 eV) and close to the bandgap energy of 1.06 eV, as discussed in Section 3.5.2. The amplitude of the change in the transient transmission trace from this film is therefore lower than for C$_{60}$.

### 3.6.3 Relaxation dynamics

The relaxation dynamics of excitations in the Li@C$_{60}$, (Li@C$_{60}$)$_2$ and C$_{60}$ films shown in Fig.3.19 follows a nonexponential decay. Several studies on the relaxation of the singlet Frenkel excitons in solid C$_{60}$ generated by the absorption at 2 eV have been reported in the literature. The nonexponential decay of the transient signal has been explained by various mechanisms, including carrier hopping [ChH92] and carrier trapping [JHS93] characteristic for disordered semiconductors, free carrier scattering [BKW92], intramolecular relaxation [FID93] and polaron formation [IIS98]. None of these approaches can accurately describe the dependence of the relaxation dynamics on the fluence of the pump beam, i.e. on the excitation density. This dependence is illustrated in Fig.3.21 for our measurements on Li@C$_{60}$ and C$_{60}$ films. The behaviour of the (Li@C$_{60}$)$_2$ film is similar to the Li@C$_{60}$ (except for the opposite sign of the transient signal). At higher pump fluence the initial decay is very fast and becomes slower as this fluence is decreased. Excitonic interactions and annihilation have to be considered in order to account for this dependence [FPB92, BKW92, DVM95, CYK99]. A consistent modelling of the nonexponential decay of the induced absorption at 2 eV based on singlet exciton - exciton annihilation processes was given by Dexheimer et al. in [DVM95]. The relaxation of the excitation was probed in this study by transient differential transmission at wavelengths in the range of 550 to 670 nm. This model is also used here to explain the relaxation dynamics of excitations generated by absorption at 2 eV in $C_{60}$, followed in our study by the transient transmission at 1250 nm, and a similar approach is used for the endohedral fullerene films.

Exciton annihilation, also called Förster annihilation process, is a nonradiative bimolecular process of the type $S_1 + S_1 \rightarrow S_0 + S_n$, in which one exciton resonantly transfers its energy to a neighbouring exciton, which is promoted in a higher-lying electronic state. The excited molecule returns via fast internal conversion from the $S_n$ state to $S_1$, resulting in an effective loss of one of the two excitons. The energy transfer rate depends on the coupling of the donor and acceptor transition dipole moments, i.e. on the molecular transitions $S_1 \rightarrow S_0$ and $S_1 \rightarrow S_n$. The interaction has a $1/R^6$ dependence on the distance between excitons, so that the exciton diffusion by a Förster resonant energy transfer $S_1 + S_0 \rightarrow S_0 + S_1$ has a critical influence on the rate of exciton annihilation.

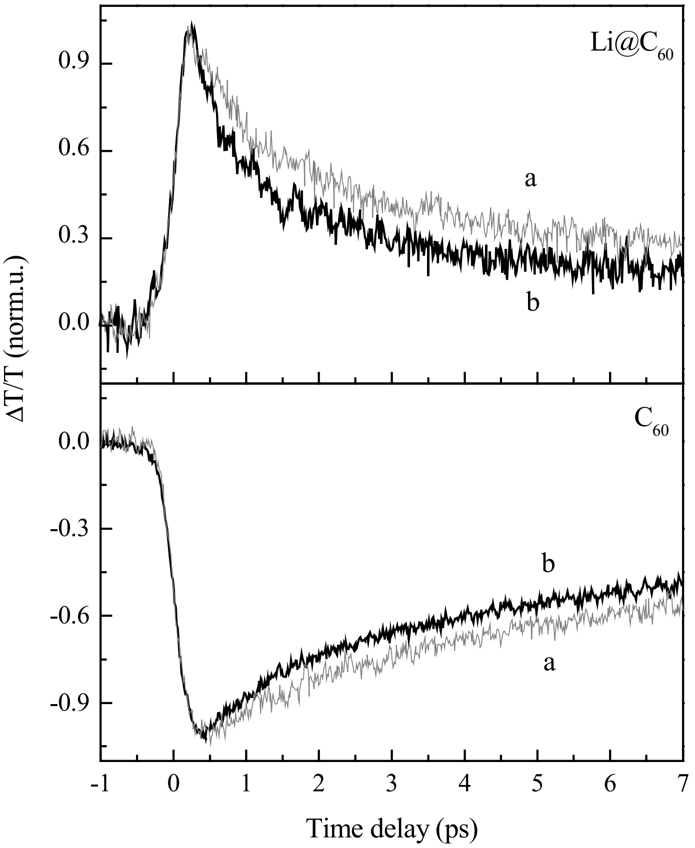

*Fig.3.21. Normalised transient differential transmittance for two laser fluences of the pump beam: (a) 3.7 mJ/cm$^2$ and (b) 7.7 mJ/cm$^2$.*

The amplitude of the differential transmission is proportional to the exciton density within the limit of small changes. The rate equation for the exciton density decay can be written (for a delta-function excitation pulse) as:

$$\frac{dn}{dt} = -\gamma \cdot n^2 - \beta \cdot n \ , \tag{3.3}$$

where $\gamma$ is a bimolecular decay constant representing the exciton-exciton annihilation rate and $\beta$ is a unimolecular decay constant. This equation can be resolved analytically and the time-dependent exciton density is found to be [THW92]:

$$n(t) = n_0 \frac{e^{-\beta \cdot t}}{1 + \frac{n_0 \cdot \gamma}{\beta}\left(1 - e^{-\beta \cdot t}\right)} \ , \tag{3.4}$$

with $n_0$ the initial exciton density at time zero. This model assumes that the excitons diffuse sufficiently fast to maintain a homogeneous random distribution of the excitons in the film. The slope of the decay of the transient signal depends only on the excitation density at a given time.

For a motion-limited exciton diffusion, the bimolecular interaction is faster than the diffusion of the excitons. The exciton annihilation rate is dominated in this case by a Förster long-range dipole-dipole interaction [För49] and by the speed at which the excitons approach each other close enough for an effective interaction, $v = \sqrt{\frac{D}{t}}$ ($D$ the diffusion constant), giving rise to an effective time-dependent annihilation rate:

$$\frac{dn}{dt} = -\frac{\gamma \cdot n^2}{\sqrt{t}} - \beta \cdot n \ . \tag{3.5}$$

This gives the following time dependence of the exciton density:

$$n(t) = n_0 \frac{e^{-\beta \cdot t}}{1 + \frac{\sqrt{\pi} \cdot \gamma \cdot n_0}{\sqrt{\beta}} erf\sqrt{\beta \cdot t}} \ , \tag{3.6}$$

where erf is the error function:

$$erf(x) = \int_0^x e^{-u^2} du \ . \tag{3.7}$$

Equation (3.6) does not only reflect the dependence of the dynamics on the total excitation density at a given moment, but also a dependence on the history of the decay following the excitation. Fig.3.22 shows a comparison of the decay at different initial excitation densities $n_0$, in which the time scale for the decay curve from lower *$n_0$* was shifted in order to overlap with the corresponding excitation density of the decay curve from higher *$n_0$*.

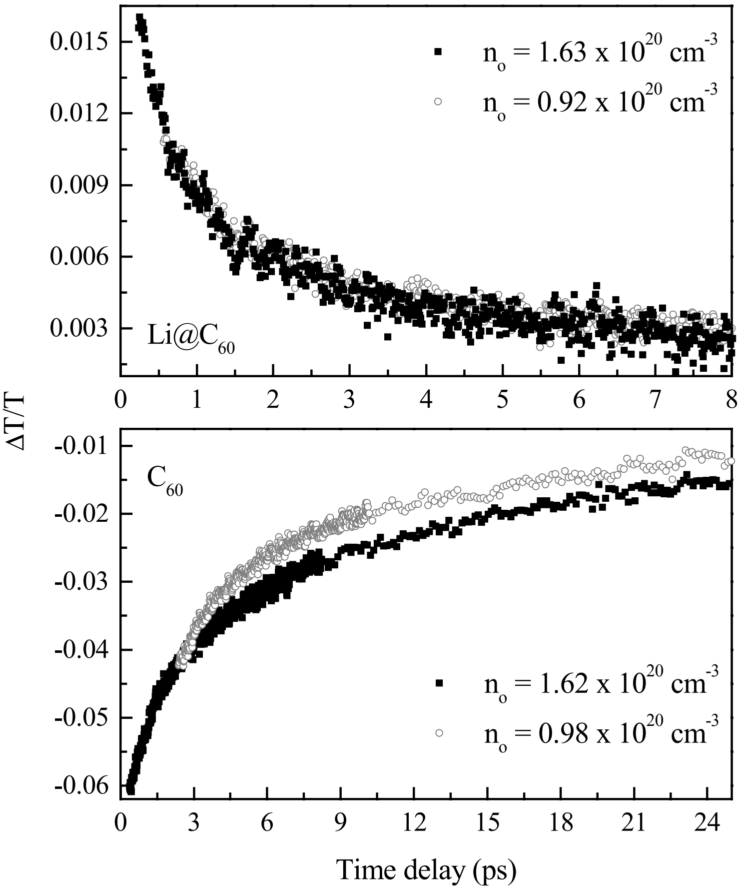

*Fig.3.22. Dependence of the differential transmission slope on the history of the relaxation, for two initial excitation densities $n_0$, for $C_{60}$ and Li@$C_{60}$ films. The curves corresponding to a lower $n_0$ are shifted in time to overlap the corresponding excitation density reached after an initial decay in the curves corresponding to a higher $n_0$.*

Obviously, the slopes at the same excitation density at a given time are unequal for the $C_{60}$ film, while the two signals overlap very well (within the noise level) for the Li@$C_{60}$ film. The (Li@$C_{60}$)$_2$, not shown here, has a similar behaviour as Li@$C_{60}$. The behaviour of the endohedral materials can be interpreted in terms of a high mobility of the excitons, giving a homogeneous random distribution of the nearest-neighbours at any given time in the films. This situation is different in $C_{60}$ films, where the mobility of the excitons is lower. Immediately after the excitation, the nearest-neighbour distance between the excitons will have a uniform random distribution. The closest neighbours will interact very fast (the long-range Förster interaction has a $1/R^6$ dependence on the distance between the excitons) and the excitons will not move fast enough in order to restore these closer distances in the nearest-neighbour distribution. Therefore, the slope of the relaxation curve will be lower (dominated by the exciton diffusion) when a certain average density is reached after an initial decay, compared to the case when the relaxation *starts* at this average density. The time-dependent annihilation rate is described in this case by equations (3.5) and (3.6), giving rise to a non-Markovian behaviour of the decay dynamics.

The difference in the mobility of the excitons between Li@$C_{60}$ and $C_{60}$ can be explained based on energetic considerations. The singlet exciton diffusion is mediated by a resonant energy transfer process $S_1 + S_0 \rightarrow S_0 + S_1$. The transition between $h_u$ ($S_0$) and $t_{1u}$ ($S_1$) levels in $C_{60}$ is dipole-forbidden, and occurs only via a weak vibrational Herzberg-Teller coupling. $S_0$ corresponds in Li@$C_{60}$ to the partially occupied $t_{1u}$ level, while the pumping with 2 eV excites the molecule to the $h_g + t_{2u}$ levels, which we could denote in this simple one-electron molecular picture as $S_2$. The transition between $t_{1u}$ and $h_g + t_{2u}$ is dipole-allowed, so one can expect a higher cross-section for the energy transfer between two adjacent molecules, leading to a higher mobility of the excitons. However, a similar explanation can not be given for the (Li@$C_{60}$)$_2$ films, where the population of the $t_{1u}$ level is not reflected in the ground-state absorption spectra. A strong intermolecular interaction is thus assumed for the endohedral materials, with a large delocalisation of the states determining a higher mobility of the excitations.

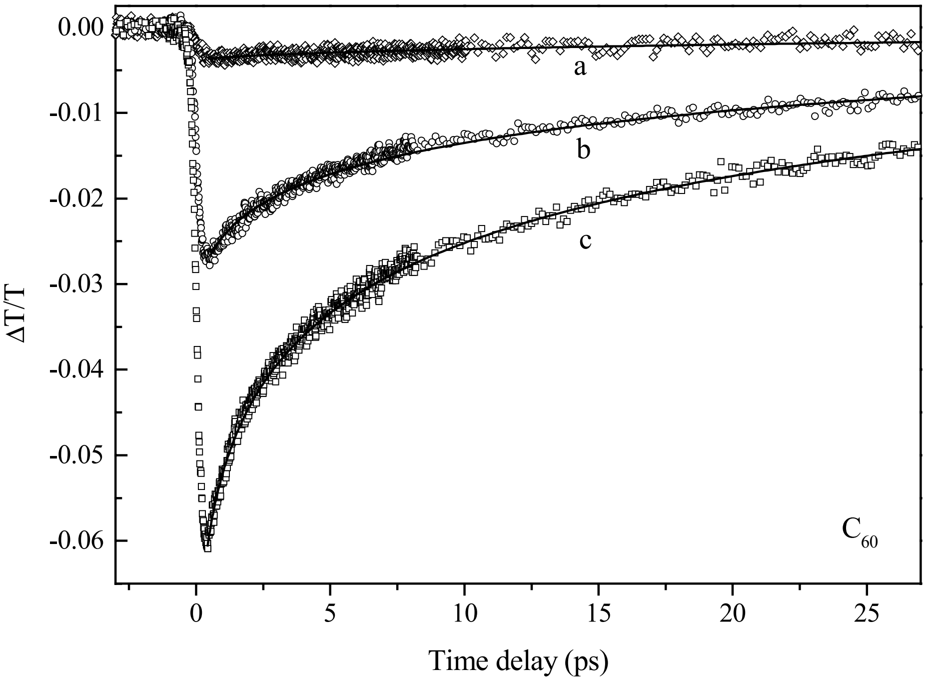

*Fig.3.23. Time-dependent differential transmission at 1250 nm from the $C_{60}$ film, for excitation densities of (a) $1.7\cdot10^{19}$ $cm^{-3}$, (b). $6.7\cdot10^{19}$ $cm^{-3}$ and (c) $1.2\cdot10^{20}$ $cm^{-3}$. The solid lines are least square fits from equation (3.6).*

The transient transmission traces from $C_{60}$ were fitted over the full time range observed for the decay (up to 150 ps), excluding the duration of the pump pulse, using equation (3.6). The fits for three excitation densities are shown in Fig.3.23. Values for the annihilation constant of $\gamma = (2.3 \pm 0.7)\cdot 10^{-15}$ cm$^3$·s$^{-1/2}$ and for the unimolecular decay constant $\beta = (1.6 \pm 0.1)\cdot 10^{10}$ s$^{-1}$ were obtained from these fits. These values compare quite well with the values reported by Dexheimer et al. [DVM95], of $\gamma = (7 \pm 1)\cdot 10^{-15}$ cm$^3$·s$^{-1/2}$ and $\beta \approx 10^{10}$ s$^{-1}$ for the same excitation followed by transient differential transmittance at 620 nm (see also Fig.3.24). The similar values of these relaxation constants, obtained in the present study with the probe at 1250 nm, indicate that the same relaxation process occurs throughout the photoexcited optical band. The small differences can arise from a different quality of the films used in the experiments, such as the dimensions of the crystalline domains or the impurities content (all experiments were performed in air, both in the present study and in [DVM95]).

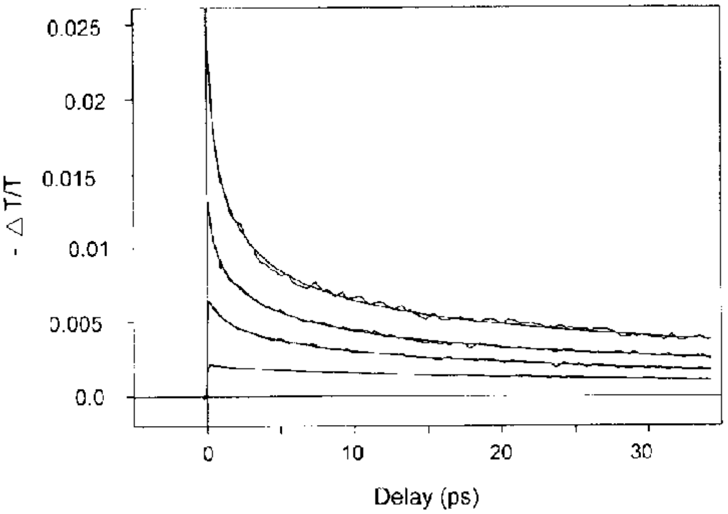

*Fig.3.24. Time-resolved negative differential transmittance at 620 nm of a $C_{60}$ thin film, following excitation at 620 nm. Excitation densities (from top): $8.1\cdot 10^{19}$, $4.4\cdot 10^{19}$, $2.1\cdot 10^{19}$ and $7.0\cdot 10^{18}$ cm$^{-3}$ [DVM95].*

The excitation decays in Li@$C_{60}$ films, which were fitted using equation (3.4), are shown in Fig.3.25 for three different excitation densities. The exciton-exciton annihilation constant obtained from these fits is $\gamma = (9.2 \pm 1.4)\cdot 10^{-9}$ cm$^3$s$^{-1}$. This value can be compared with results from other extended π-electron systems (conjugated polymers). The annihilation constants reported for films of poly(p-phenylenevinylene), $\gamma = 4\cdot 10^{-8}$ cm$^3$s$^{-1}$ [KVJ96] and $2.4\cdot 10^{-9}$ cm$^3$s$^{-1}$ [DTS99] are similar, but the value reported for conductive films of fluoro-aluminium phthalocyanine films, of $3.5\cdot 10^{-7}$ cm$^3$s$^{-1}$ [HoP88] is much larger. The annihilation constant $\gamma$ depends both on the diffusion rate of the excitons and on the effective interaction distance between the excitons. Additional measurements are necessary in order to distinguish between these two parameters. The relaxation decay in Li@C$_{60}$ is dominated by the strong exciton annihilation process within the first 10 ps after excitation, and the unimolecular decay constant $\beta$ was irrelevant for the fits for values lower than ~ $7\cdot10^{10}$ s$^{-1}$. After ~ 13 ps all curves have reached the same level of the differential transmission (equivalent to an excitation density of ~ $1.7\cdot10^{19}$ cm$^{-3}$) and follow a decay dominated by the unimolecular process. A single exponential fit of this decay gives a more accurate value for the unimolecular decay constant of $\beta = (4 \pm 2)\cdot10^{10}$ s$^{-1}$, which is slightly higher than the value measured for C$_{60}$.

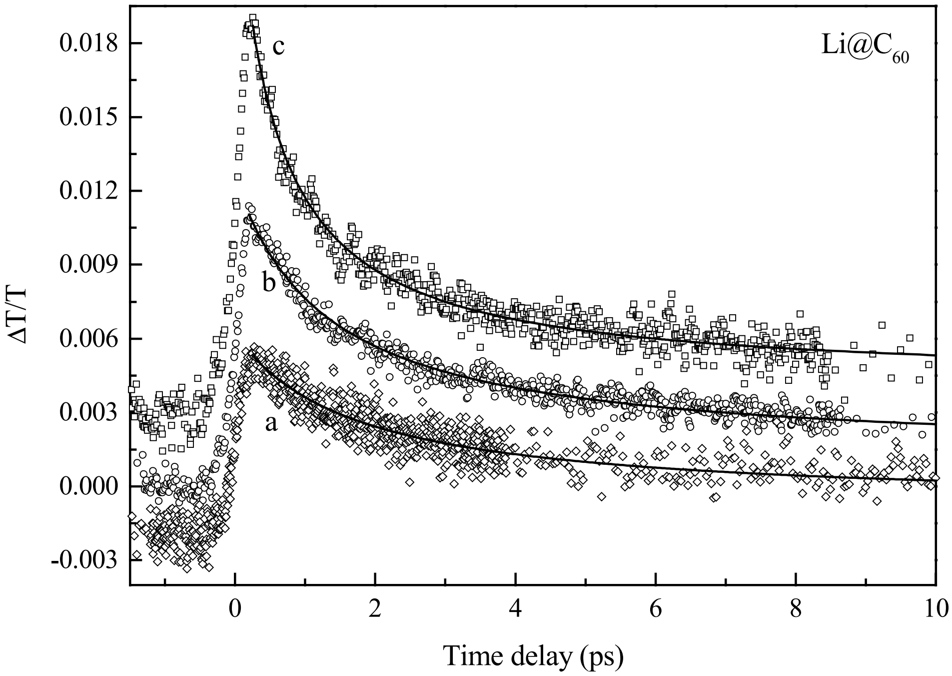

*Fig.3.25. Time-dependent differential transmission from the Li@C$_{60}$ film, for initial excitation densities of: (a) $5.4\cdot10^{19}$ cm$^{-3}$, (b) $9.1\cdot10^{19}$ cm$^{-3}$ and (c) $1.63\cdot10^{20}$ cm$^{-3}$. The solid lines are best fits using equation (3.4). The curves (a) and (c) are shifted in intensity, for better clarity.*

Although the simple model of exciton-exciton annihilation seems to describe reasonably well the experimental data, we have not included here an additional possible decay channel, from the $h_g + t_{2u}$ levels (S$_2$) to the intermediate $t_{1g}$ (or S$_1$) level. If the absorption cross-sections at the probe wavelength of 1 eV were similar for this level and e.g. the $t_{1u}$ (S$_0$) level, this additional decay channel would not be reflected in the present measurements. Additional measurements with different probe wavelengths are necessary to investigate this possibility.

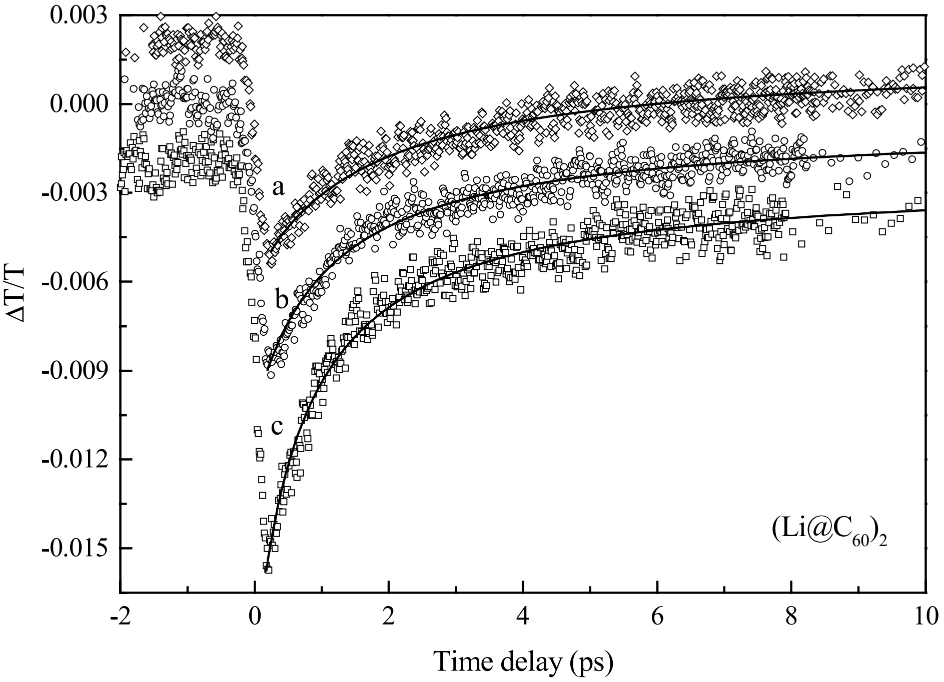

*Fig.3.26. Differential transmission from the film of* $(Li@C_{60})_2$ *for the initial excitation densities: (a)* $6.1\cdot10^{19}$ $cm^{-3}$*, (b)* $8.6\cdot10^{19}$ $cm^{-3}$ *and (c)* $1.7\cdot10^{20}$ $cm^{-3}$*. Solid lines are best fits using equation (3.4). The curves (a) and (c) are shifted in intensity for a clear presentation.*

The transient differential transmission for three initial excitation densities in the $(Li@C_{60})_2$ film is shown in Fig.3.26, together with the best fits using equation (3.4). A value of $(9.7 \pm 1.5)\cdot10^{-9}$ $cm^3s^{-1}$ was obtained from the fits for the annihilation constant $\gamma$, equal to the constant found for the $Li@C_{60}$ material. The bimolecular exciton annihilation process is, in this case, dominating the decay down to an excitation density where the change in the transmittance is not distinguishable from the noise level. This can be an indication for a longer lifetime of the isolated exciton compared to the values found for $C_{60}$ and $Li@C_{60}$. No accurate value for the unimolecular decay constant $\beta$ could be obtained for this material.

## 3.7 $Li@C_{60}$ photopolymerisation

### 3.7.1 Phototransformation kinetics studied by SHG

The kinetics of phototransformation in $Li@C_{60}$ thin films was measured using second harmonic generation. The experimental setup for these measurements was presented in Chapter 2.3. The films of $Li@C_{60}$ were produced with a constant heating rate of 10 K/s using the transfer evaporator described in 3.4.2. Once the temperature raised above 350 °C the evaporator was moved from a distance of 300 mm to 5 mm in front of the substrate. Prior to the deposition, the material was degassed by heating at 70 °C in the load-lock chamber at a pressure of $5 \times 10^{-8}$ mbar, for 12 hours. The Li@$C_{60}$ films were about 1 μm thick (as measured with atomic force microscopy) and amorphous - no LEED pattern can be observed even for thinner films. The phototransformation kinetics was studied in situ, at a base pressure of $1 \cdot 10^{-10}$ mbar. Any exposure to ambient light was carefully avoided. The films were irradiated under the same conditions used for the $C_{60}$ films, with an $Ar^+$ laser at 514 nm and 320 $mW/cm^2$ power density.

Although the SH signal intensity from the 1 μm Li@$C_{60}$ film was comparable to the 650 nm $C_{60}$ film, no meaningful comparison of the SHG efficiencies of both materials can be given. The Li@$C_{60}$ has different linear and nonlinear optical constants compared to the $C_{60}$. A strong absorbance at the fundamental wavelength (1064 nm) was measured due to the charge transfer from the Li atom to the fullerene cage, compared to $C_{60}$, which is transparent at this wavelength (see also Section 3.4.3). Furthermore, SHG in a thin film geometry exhibits a complicated interference pattern with the thickness of the film, which depends on both linear and nonlinear optical properties of the materials at the fundamental and the second harmonic wavelengths (see also the discussion in Chapter 2.3.1). Our discussion is therefore restricted to the influence of the $Ar^+$ laser irradiation on the SH response from the Li@$C_{60}$ films.

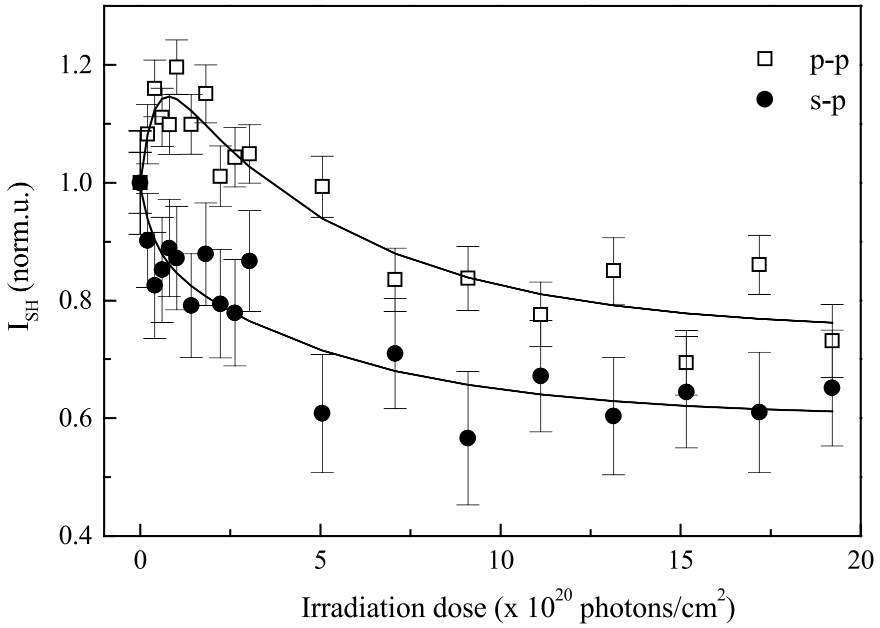

*Fig.3.27. Second harmonic signal from a Li@$C_{60}$ film as a function of the $Ar^+$-laser irradiation dose. The signal is normalised to the SH signal of the not irradiated film.*

The SH signal from Li@$C_{60}$ as a function of the $Ar^+$ laser irradiation in Fig.3.27 shows a double exponential behaviour similar to the $C_{60}$ (see Chapter 2.5.2). For the Li@$C_{60}$ film, there is a maximum in the p-p and not in the s-p polarisation combination, in contrast to the $C_{60}$ film. This difference is due to the different relative phases of the complex coefficients describing the SHG efficiency of the films under transformation. These different relative phases of the complex coefficients determine the apparent different behaviour of the p-p and s-p signals in Fig.3.27. The exponential behaviour is, though, the same for both s-p and p-p polarization combinations and reflects the transformation kinetics of the film by irradiation. The irradiation constants from the exponential fits (using equation 2.15), listed in Table 3.2, are only slightly lower than in the case of $C_{60}$ and the amplitude of the change in the SHG is smaller.

| | Li@$C_{60}$ (~ 1 μm) | $C_{60}$ (0.65 μm) |
|---|---|---|
| $\delta_1$ ($\cdot 10^{20}$ photons/$cm^2$) | 0.4 | 0.5 |
| $\delta_2$ ($\cdot 10^{20}$ photons/$cm^2$) | 5.7 | 8.7 |

*Table 3.2. Exponential constants of the double exponential change in the SH signal from Li@$C_{60}$ and $C_{60}$ films, induced by laser irradiation at 514 nm wavelength.*

The transformed material was further investigated with different methods, in order to clarify the nature of this phototransformation. The UV-VIS absorption spectra of the Li@$C_{60}$ films were not affected by irradiation with $3\cdot 10^{21}$ photons/$cm^2$.

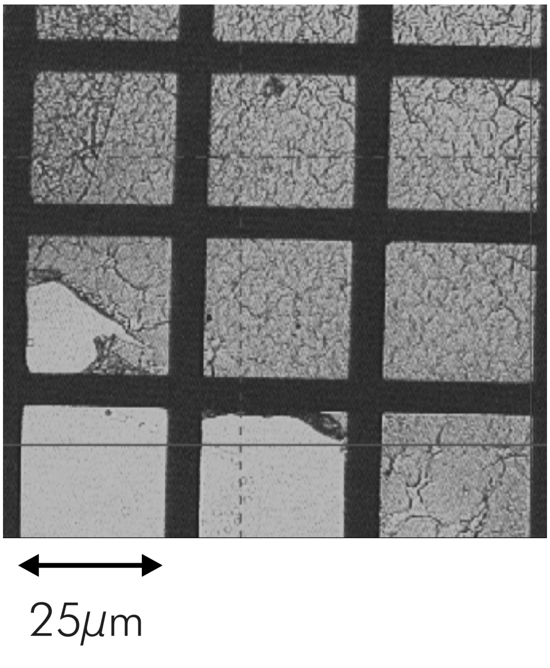

*Fig.3.28. Optical micrograph of a membrane of polymerised Li@$C_{60}$, with a thickness of ~ 1 μm*

The irradiated film was not soluble in ODBC anymore. This result is considered as a first evidence for the photopolymerisation of the material. The polymerised sections were floating from the Ni(111) surface into the solvent in membranes of 1-2 mm diameter. A few pieces were collected on copper grids and studied under a transmission electron microscope (TEM).

Electron diffraction confirmed the amorphous structure for the film, while the TEM and optical microscopic images (Fig.3.28) showed the membranes to be homogeneous and compact, an indication for the formation of randomly oriented bonds in the irradiated film.

## 3.7.2 IR absorption of photoirradiated Li@$C_{60}$

The changes induced by phototransformation in the IR spectra of Li@$C_{60}$ films are relatively small. Absorption difference spectra were determined by subtracting the absorption spectrum of the pristine film from the spectrum measured after irradiation. The spectrum of a film irradiated with $0.4 \cdot 10^{20}$ photons/cm$^2$ (the lower exponential constant from the transformation kinetics) was showing no significant changes in the IR spectrum compared to the pristine film and therefore is not shown here.

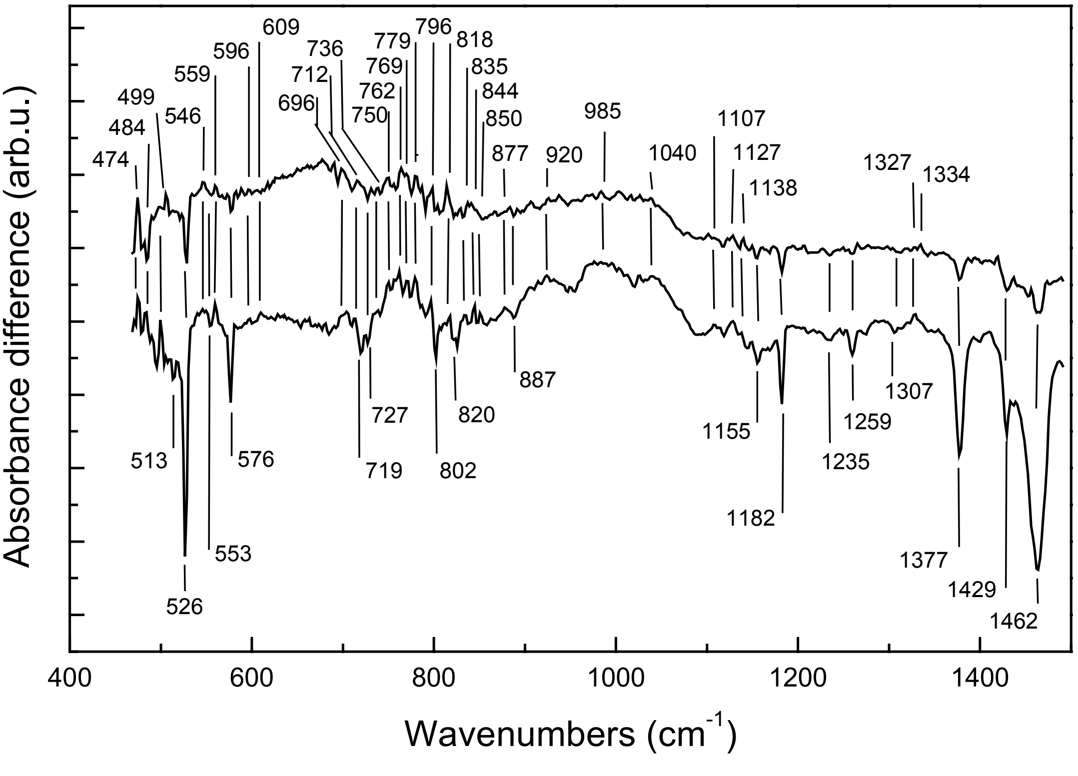

*Fig.3.29. Difference IR spectra of Li@$C_{60}$ films irradiated with $6 \cdot 10^{20}$ photons/cm$^2$ (upper spectrum) and $1.4 \cdot 10^{22}$ photons/cm$^2$ (lower spectrum). The modes of the pristine material, decreasing due to irradiation, are marked in the lower part of the figure. The new peaks are marked in the upper part of the figure.*

Fig.3.29 shows the IR absorption difference spectra of a film irradiated with $6\cdot10^{20}$ photons/cm$^2$ and $1.4\cdot10^{22}$ photons/cm$^2$, respectively. The higher dose was chosen in order to identify changes in the vibrational spectra with certainty. Nevertheless, polymeric modes are clearly visible for the spectrum measured at the lower dose in Fig.3.29. The negative peaks marked in the lower part of the figure are due to a reduction of the absorption seen in the pristine Li@C$_{60}$. The peaks at 513, 719, 727, 887, 1155, 1377 and 1462 cm$^{-1}$ are characteristic absorption frequencies for the Li@C$_{60}$ films, together with the peaks at 526, 576, 1182, 1429, 1235, 1259 and 1307 cm$^{-1}$, which are also found for pristine C$_{60}$.

Several new modes appear after irradiation, identified as positive peaks in the upper part of the difference spectrum. These irradiation-induced modes are seen already in the spectrum of the film irradiated with $6\cdot10^{20}$ photons/cm$^2$, and are enhanced when increasing the irradiation dose. The peaks at 484, 546, 559, 596, 609, 696, 704, 712, 736, 762, 769, 779, 796 and 877 cm$^{-1}$ correspond to polymeric peaks in C$_{60}$ [RZW93, MMS98, OnT96]. The two peaks at 818 and 835 cm$^{-1}$ could be referred to similar peaks found for dimeric Rb-doped C$_{60}$ [MKR95]. Several other peaks at 474, 499, 844, 850, 862, 1107, 1127, 1327 cm$^{-1}$ and the broad absorptions centered at 920, 985 and 1040 cm$^{-1}$ can not be identified with IR spectra of polymerised fullerene materials in the literature.

## 3.7.3 TDS of photoirradiated films

Thermal desorption spectrometry was performed under the experimental conditions described in Chapter 2.3.2 on vapour-deposited films of Li@C$_{60}$ irradiated with $5\cdot10^{21}$ photons/cm$^2$. The ratio of endohedral to empty fullerenes for these films is $R = (9.9 \pm 1.0)\%$, equal to the $(9.8 \pm 1.0)\%$ found for the not irradiated films. This shows that the laser irradiation at 514 nm does not induce the decay of the endohedral Li@C$_{60}$ into C$_{60}$.

A comparison between the temperature-programmed desorption (TPD) traces of Li@C$_{60}$ from an irradiated film and a not-irradiated film is given in Fig.3.30. The desorption of Li@C$_{60}$ is initiated at slightly higher temperatures for the irradiated film. A broad shoulder at higher temperatures can be observed in this trace, indicating that a new phase, with higher binding energy, was formed by the irradiation of the molecules in the film. The temperature corresponding to this peak, of ~ 500 °C, is fairly close the second Li@C$_{60}$ peak at 540 °C temperature in the direct desorption of the material that was dried from solution (described in Chapter 3.4.2). This peak was tentatively assigned to "aggregates" of Li@C$_{60}$. No absolute comparison of the two temperatures can be made, since it is well known [e.g. Men75] that for zeroth-order desorption kinetics (consistent with the desorption of $C_{60}$ multilayers [THG91, KKT98]), the peak temperature in the TPD trace moves to higher temperatures when the initial amount of adsorbates or the thickness of the films is increased. Thus, the slightly lower peak temperature found for the irradiated films could simply mean that the total amount of polymerised material is lower than the total content of "aggregates" in the solution-dried films. Such a conclusion would imply that the desorption of Li@$C_{60}$ is following a zeroth-order desorption kinetics. The poor control of the film thickness and the purity of the material in these measurements does not allow, though, a systematic analysis of the desorption kinetics for the endohedral molecules. Another explanation for the difference between these two temperatures can intuitively be given if we assume that the bond type between the Li@$C_{60}$ molecules is different for the photopolymers and for the aggregates formed in solution, respectively.

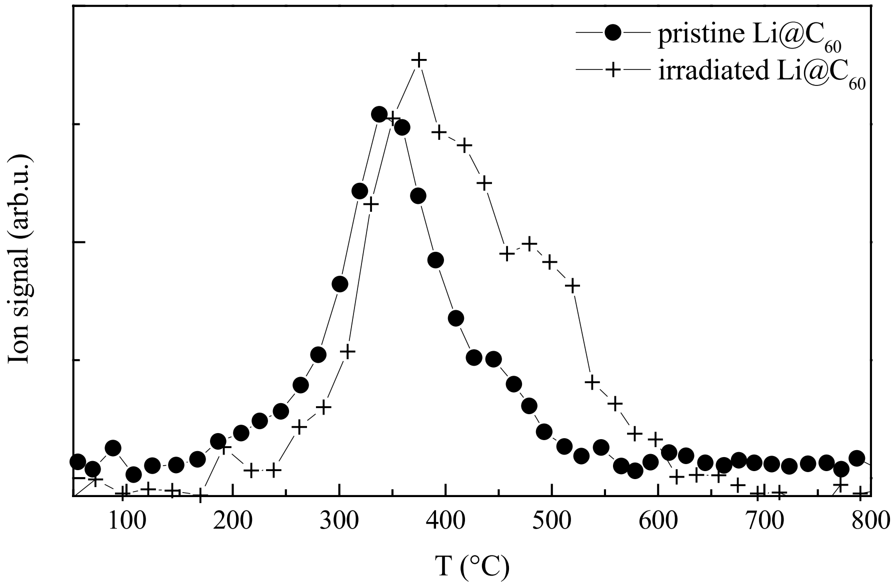

*Fig.3.30. Thermal desorption signal of Li@$C_{60}$ from a not-irradiated film (circles) and from a film irradiated with $5 \cdot 10^{21}$ photons/cm$^2$ (crosses).*

The IR absorption peaks measured in the region of 700-800 cm$^{-1}$, the insolubility of the irradiated films and the desorption of endohedral species with higher binding energy after irradiation are clear evidence for Li@$C_{60}$ photopolymerisation. The fact that the transformation kinetics is fairly similar to $C_{60}$ is opening the question about the structure of polymerised Li@$C_{60}$. A linear long-range order, which was found in the case of Rb-doped $C_{60}$ films [ERZ95] due to polymeric chains, was not observed for Li@$C_{60}$. Theoretical calculations, assuming an intramolecular charge transfer from the Li to the $C_{60}$ cage, indicate that the formation of dimers with a single intermolecular bond (shown in Fig.3.31) is an exothermic reaction of –19.4 kcal/mol [MCH98].

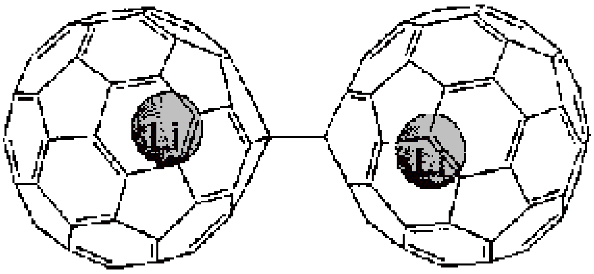

*Fig.3.31. Intermolecular bonding in Li@$C_{60}$ dimer [MCH98]*

Dimer formation was found from the endohedral production process, as already mentioned in Section 3.2 [Kra98]. While the IR absorption spectrum of droplet-deposited films of the dimeric fraction is distinct from the spectrum of the monomeric fraction, no significant differences could be identified in the IR absorption spectra measured from vapour-deposited films. The optical absorption spectra, though, are markedly different between the two vapour-deposited materials, showing that the molecules still preserve their different structure after (see discussion below, in Section 3.7). From the similarity of the photoirradiation-induced IR absorption peaks in Li@$C_{60}$ with the polymeric $C_{60}$ peaks, we conclude that 2+2 cycloaddition is a very probable scheme for oligomerisation reactions.

## 3.8 Conclusions

The endohedral fullerene Li@$C_{60}$ is a thermally stable molecule, which can be deposited as thin films by sublimation. Some of the material is lost during heating when the Li@$C_{60}$ is transformed to an insoluble and not sublimable state. The loss can be attributed both to a thermal polymerisation of the molecules and to a total destruction of the cage catalysed by intercalated solvent molecules and impurities. High heating rates are favourable for the sublimation and no fragmentation of the Li@$C_{60}$ to $C_{60}$ was observed from Li@$C_{60}$ films deposited with high heating rates.

The optical properties of vapour-deposited films of Li@$C_{60}$ have been investigated. The IR absoption spectrum shows a series of new peaks compared to the empty fullerene, which are in good agreement with the theoretical predictions.

The dimer fraction $(Li@C_{60})_2$ forms a semiconducting molecular solid, which is reflected in the UV-VIS absorption spectrum. A bandgap of 1.06 eV was calculated from the dependence of the absorption on the photon energy, in the region of the fundamental absorption edge. A strong absorption centered at 1.1 eV measured from vapour-deposited films of the Li@$C_{60}$ monomer is giving a good indication for an intramolecular charge transfer form the Li 2s orbital to the LUMO of the fullerene cage. The absorption peaks in these solid materials are broadened and red-shifted, compared to their absorptions in solutions, which is indicating a strong intermolecular interaction in the solid state.

The relaxation dynamics of excitons in Li@$C_{60}$ was studied with a two-colours pump-probe technique using a Cr:forsterite laser (1 kHz,155 fs) at 1250 nm and 625 nm wavelength, built at MBI. The measurements showed a transient absorption for $C_{60}$ but a transient bleaching of the absorption for Li@$C_{60}$. This difference in the behaviour can be explained based on the Li to $C_{60}$ charge transfer using DOS calculations by Broclawik and Eilmes [BrE98]. The relaxation in Li@$C_{60}$ films is faster than for the $C_{60}$ films and follows a nonexponential decay. Measurements at different excitation fluences have shown that the decay obseved is consistent with a dominating exciton-exciton annihilation process. The annihilation and unimolecular relaxation constants obtained from the fits of the transient signals are listed in Table 3.3.

| | Annihilation constant $\gamma$ | Unimolecular decay constant $\beta$ |
|---|---|---|
| Li@$C_{60}$ | $(9.2 \pm 1.4)\cdot 10^{-9}$ $cm^3s^{-1}$ | $(4 \pm 2)\cdot 10^{10}$ $s^{-1}$ |
| (Li@$C_{60})_2$ | $(9.7 \pm 1.5)\cdot 10^{-9}$ $cm^3s^{-1}$ | $< 10^{10}$ $s^{-1}$ |
| $C_{60}$ | $(2.3 \pm 0.7)\cdot 10^{-15}$ $cm^3s^{-1/2}$ | $(1.6 \pm 0.1)\cdot 10^{10}$ $s^{-1}$ |

*Table 3.3. Annihilation constants $\gamma$ and unimolecular decay constants $\beta$ obtained from the best fits of the transient differential transmittance for films of Li@$C_{60}$, (Li@$C_{60})_2$ and $C_{60}$.*

The annihilation constant is time-dependent for $C_{60}$, consistent with a motion-limited exciton diffusion in these films. At ~ 0.06 ps after the excitation, the rate of the exciton-exciton annihilation is the same in both materials. The rate of this bimolecular interaction decreases with time in $C_{60}$ due to a lower mobility of the excitons. A higher mobility of the excitons in Li@$C_{60}$ can be deduced from these measurements.

The transformation of Li@$C_{60}$ by laser irradiation at 514 nm wavelength using similar photon doses compared to $C_{60}$ was measured with SHG. Photopolymerisation was confirmed based on solubility tests in ODBC solvent, IR absorption spectroscopy and TDS measurements. New IR peaks, some with frequencies similar to the $C_{60}$ polymer modes, were measured for the irradiated film. Transformation kinetics is biexponential with irradiation dose constants (0.4 ± 0.2) and $(5.7 \pm 0.2)\cdot 10^{20}$ photons/$cm^2$ similar to $C_{60}$, which indicates the relevance of a 2+2 cycloaddition scheme for the polymerisation of Li@$C_{60}$.